Numerical and experimental methods applied to human exposure to electromagnetic fields

Numerical and experimental methods applied to human exposure to electromagnetic fields

Wencui Wang

Dipartimento Energia – XXV ciclo

Politecnico di Torino

Tutore
prof. Mario Chiampi
ing. Oriano Bottauscio

Coordinatore del corso di dottorato
prof. Mario Chiampi

PhilosophiæDoctor (PhD) Thesis

February 2013

Abstract

The research focuses on a hybrid experimental-numerical technique, based on Boundary Element Method (BEM), to reconstruct the electromagnetic field distribution in the space surrounding unknown sources, in both low and high frequency range. The same procedure also allows to evaluate the induced electric field non-invasively when human body presents near such sources.

By applying BEM (including Green function) to a discretized surface that enclosing the sources, the electromagnetic fields outside the surface (source free region) can be received from an integration of same quantities over this surface. At low frequency range (up to 100 kHz), the induced electric field inside human body can be also calculated as an inverse process, i.e. applying again BEM over a discrete body surface on which the magnetic fields are provided through the above procedure, to compute the fields at any point inside this surface. The only approximation during this procedure is assuming that on each discrete element, the field values are uniform. Measurement can be performed on a grid with regular step over any known surfaces and both the magnitude and phase are required for each component of the electric and magnetic fields.

The experimental validation at low frequency range has been carried out around a Helmholtz coil system enclosed by a wooden frame, which is used to position the 3D magnetic field probe. Numerous field distributions can be generated through this system by separately imposing the currents which supply the two coils, and three of them are applied in the validation procedure. The three voltage signals detected by the field meter (corresponding to the three components of the magnetic fields) are sampled synchronously with the fourth one, which is picked up from the supply circuit and acts like

a trigger, in order to compute the phases of the other three signals. The measured data is fitted by an interpolation/extrapolation technique before adopted as input for BEM reconstruction in free space.

Reconstruction quality through proposed BEM procedure has been investigated through different approaches, as well as the accuracy of the induced electric field evaluation inside the human body. Measurement uncertainty propagation has been estimated through Monte Carlo method coupled with a discrete numerical technique.

At last, the prediction of the radiation emission generated by a radio frequency model has been also presented, as an example of application for the proposed field reconstruction in high frequency ($\leq$300 MHz). A satisfactory accuracy is obtained through the comparison with another numerical method.

Acknowledgements

I would like to acknowledge the full support I received from all my colleagues working in INRIM and Politecnico di Torino, my special thank must be given to the following people: Dr. Gabriella Crotti, Dr. Michele Borsero, Dr. Domenico Giordano, Dr. Luca Zilberti, Dr.Mauro Zucca, Mr. Andrea Agosto, Mr. Luca Martino and Dr. Roberto Forastiere.I appreciate very much also the help from Dr. Patrizio Ansalone about Matlab and Latex.

Contents

List of Figures

List of Tables

LIST OF TABLES

1

Introduction

The safety concerns regarding biological effects for both occupational and public exposure to electromangetic fields(EMF) arise with the development of electrical, electronic and electro-optics devices. This subject involves technologies in different research fields such as bioelectromagnetics, radiation dosimetry, and biomedicine. From electromagnetic engineering point of view, there are two problems to be solved: what is the electric field (EF), magnetic field (MF) or electromagnetic field environments of the exposure and what is the corresponding (thermal or non-thermal) interaction with biological tissues inside living systems.

While the relative magnetic permeability is always unitary, the electric properties of biological materials, conductivity and permittivity, vary from extremely low frequency (ELF) up to Radio Frequency (RF). In low frequency range (<1 kHz), it has been validated that the displacement currents are negligible, and the living body can be considered as good conductor. Most of the exposure happens near magnetic sources (e.g. MRI scanner), where the induced currents (eddy currents) and electric fields inside the body do not modify the external (environmental) fields. The only significant exposure sources of electric field are power lines. In this case, the external fields are perturbed since only the normal components of induced electric fields exist over the body surface.

When frequency increases, the dielectric constant drops rapidly (10^5 times from 10 Hz to 10^{10} Hz in muscle) [1], and the losses in energy cannot be neglected anymore. At radio/microwave frequency frequency, the *skin effect* of a bulk of homogeneous material

can be expressed by means of penetration depth [2]:

$$\delta = (\frac{1}{\omega})\{(\frac{\mu\varepsilon}{2})[(1+p^2)^{1/2}-1]\}^{1/2} \tag{1.1}$$

where $p = \sigma/\omega\varepsilon$ is the ratio of the amplitudes of the conduction current to the displacement current. Eq. 1.1 suggests that, the penetration to certain material reduces significantly with the rise of frequency. It implies that if a human being, for instance, is submitted to a microwave field, the internal organs are more protected at higher than lower frequencies [3]. It is easy to deduce the *skin effect* of good conductors ($\sigma \ll \omega\varepsilon$) from Eq. 1.1.

The interaction mechanism of heterogeneous materials, which are more close to living systems, is much more complicated and not further discussed here, since the primary goal of this work is to evaluate the accuracy of induced field assessment inside human body through the proposed methods, rather than an investigation of specified influence of exposure on tissues or certain part of the body.

1.1 Human exposure

1.1.1 Guidelines and Standards

According to studies on both direct and indirect effects of EMF, there is no compelling evidence that chronic affects would be caused from low-frequency exposure. Anyhow, it has been well-proved that acute affects exists at muscle tissue, peripheral nervous system (perception) and central nervous system (discomfort and pain) [4, 5], especially retina (induction of magnetic phosphenes)[6]. At higher frequency ($\geq$100 kHz), the rise of temperature in tissues and over body surface become the prevailing biological effects.

Based on the results of laboratory and epidemiologica studies, International Commission on Non-Ionizing Radiation Protection (ICNIRP) has proposed the limits (basic restrictions and reference levels) to avoid adverse health effects for both occupational and public exposure[7]. Basic restrictions are given in terms of electric field (1 Hz to 100 kHz), SAR (specific energy absorption rate) and power density at radio frequency range (up to 300 GHz), defined as functions of frequency and various from different parts of human body and tissues. In the meanwhile, for practical assessment, reference levels are set based on measurable quantities (electric field strength E, magnetic

field strength H, magnetic flux density **B** and power density **S**), derived from basic restrictions and estimated through mathematical modeling, by assuming a maximum coupling of the field to the exposed individual[8].

As for the exposure to static magnetic fields, limits are provided directly in terms of magnetic flux density. Sensory effects due to the movement in the field can be minimized or avoided by complying with basic restrictions set in the ELF guidelines[9].

International and domestic organizations working on standardization such as International Electrotechnical Commission (IEC), National Radiological Protection Board (NRPB) in UK and European Committee for Electrotechnical Standardization (CENELEC), prepare and publish standards and principles for modeling procedure to assess the internal fields through environmental fields that the human model exposed to, since they can hardly be measured directly *in vivo*.

In low frequency range, both analytical and numerical models are developed for this purpose. Analytical models are in simple shape with homogeneous material, usually used for a preliminary investigation on the interaction with uniform applied field and limits for safe exposure. Numerical models provide a relatively accurate solution, which enables the detailed examination of local internal fields. In most of the cases, electrical conductivity $\sigma = 0.2$ S/m and relative electrical permittivity $\varepsilon_r = 10^5$ are adopted for field assessment for homogeneous human models.

In fact, more sophisticated results can be calculated from anatomical models (designed mostly according to[10]). This kind of computation, however, is not widely available because of the high competences requirement of software.

1.1.2 Assessment methods related to human exposure at LF

Techniques developed to evaluate the induced fields and current densities fall into two categories. One of them involves direct measurements inside or over the surface of human models.

In late 70', hollow conducting models were developed to measure surface electric fields and total induced currents[11, 12]. Almost in the same period, current densities inside homogeneous human models were also investigated through measurement [13]. These researches all dedicate to high voltage exposure under power frequency transmission line.

Affords have also been made on the measurements of internal fields and induced currents under periodic magnetic fields, e.g.[14]. With the development of magnetic resonance imaging (MRI) techniques, more attention has been payed on biological effects caused by high static magnetic fields and switching gradients when patients and health care workers staying near or inside MRI scanners. Measurements on electric fields due to temporally time-varying magnetic fields have been performed and discussed in [15]. Surface electric fields have been firstly measured on a human subject moving near the MRI scanner through dipole electric field probe [16].

However, a more common approach is to infer internal electric fields and current densities via numerical modeling. By solving Maxwell equations, various numerical methods are applied on the assessment of induced quantities, such as the scalar potential finite difference (SPFD) technique[17], finite difference time domain method (FDTD)[18], finite integration technique (FIT)[19], boundary element method (BEM)[20], etc. There were also numerical calculations making use of three-dimensional impedances method[21, 22].

Although, most of these methods have the assumption that the applied field distributions are given or the EM sources are wholly identified, which is not always feasible for practical exposure conditions.

In this work, the internal electric field distributions are estimated inside a human model exposed to unknown sources, through a set of measurements over a virtual surface that encloses all the sources. Thus, two independent steps are needed for this procedure:

1) reconstruct the field distribution generated from unknown electromagnetic sources;

2) calculate the induced electric fields through the field distributions over the surface of human model.

The two steps can be separated to solve two different problems, and each of them involves BEM. At low frequency range, the internal electric field vectors induced from the reconstructed magnetic fields will be evaluated and verified, followed by uncertainty estimate procedure based on Monte Carlo Method. This method is no longer suitable in high frequency exposure assessment due to the strong coupling between internal and external fields of the human model.

1.2 Source Identification

Source identification refers to the techniques of locating and assessing the electromagnetic sources[23, 24]. It can be applied when invasive measurements are not allowed *in vivo* [25, 26], or when the fields generated from electronic appliances must be design and optimized[27, 28]or estimated[29, 30] in order to prevent potential harm of human exposure or possible damage to other devices. For the last application, a general target is to estimate the field distributions rather than identify or localize the sources.

Usually, source identification procedure requires introducing fictitious elementary dipoles or multipoles to substitute the real sources by solving an inverse problem. The procedure proposed in this work takes advantage of the well-known capability of BEM of reconstructing the electromagnetic field distributions generated from unknown sources starting from the knowledge of the fields on a finite number of points[31], without the requirement of time-consuming optimization process.

This procedure has been verified both numerically and experimentally at low frequency range, by reconstructing the magnetic fields around the sources whose field distributions are well controlled, in order to bring convenience for the accuracy evaluation. The uncertainties of the reconstructed fields through the measurements over a parallelepiped has been investigated, together with the induced electric fields calculation procedure, since these two procedures are jointed for the assessment of internal fields of human model exposed to unknown fields.

1.3 Application in high frequency

The estimation of radiation emissions is one of the major subjects of electromagnetic compatibility (EMC). Standards set the limits for the emissions in order to protect electronic devices from malfunction[32, 33] and avoid heating problems regarding human exposure[34].

In general, the '$1/d$' law of propagation can be applied to calculate the field values at different distance d from the sources, although this method is only valid in far-field condition. The alternative method is to reconstruct the fields around the sources by near-field measurements [35, 36]. Reference [37] provides a relatively precise deduction of the field distributions starting from the fields over some sphere that includes all the radiation sources, which has been adopted by Standard CEI EN 50383.

The proposed procedure in this work is capable to perform an accurate reconstruction of electromagnetic fields in free space, requiring limited number of measurement points (same as or less than source identification techniques), even though an approximation of BEM must be introduced. The accuracy of the reconstructed fields will be evaluated numerically. Experimental validation is not available at the moment due to the limitation radio frequency electric field probe, since both amplitude and phase for each field component are necessary to complete the reconstruction.

2

A BEM application

2.1 Introduction

This chapter explains theoretically the field computation starting from complex form of Maxwell equations, and the procedure that makes use of the intrinsic property of BEM to solve field problems.

2.1.1 Boundary Element discretization

The aim of the numerical approach is to establish relations between the electromagnetic field distribution in free space or inside human body and the knowledge of fields over the discretized boundary surface. Figure. 2.1 shows the approximation procedure of the boundary geometry in 2D (Figure. 2.1a) and 3D(Figure. 2.1b) respectively.

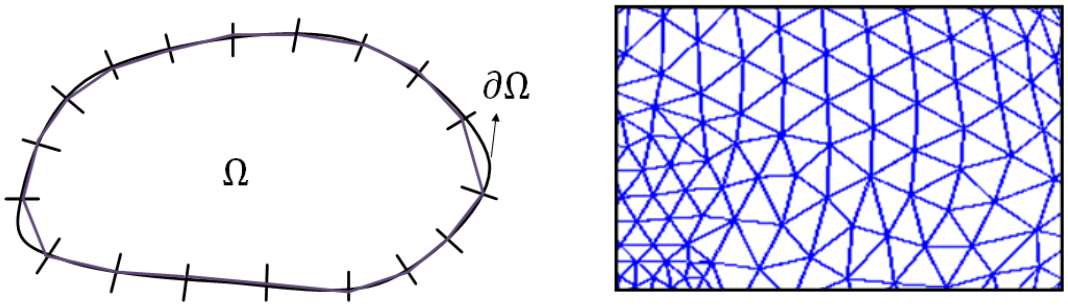

Figure 2.1: Boundary approximation in 2-Dimensional and 3-Dimensional situation

Firstly, the irregular boundary is divided into a set of sub-boundaries, and then, replaced with more regular and simple geometry (segments in 2D and triangles or quadrangles in 3D) for each of them. Next step is to assign the electric field and magnetic field vectors for the discretized boundary. Different approaches can be applied on this step, a simple one to find out a proper constant for each of them. The fields on the midpoint of the segments or the barycenter of the triangles or quadrangles are usually chosen for this purpose. Finally, the integration over the surface can be approximately expressed through a summation based on these boundary elements.

Therefore, the fundamental requirement is the field vectors on the specified points (midpoint of barycenter) in order to proceed. Apparently, with more elements, better approximation can be expected. However, on the other side, the measurements on the specified points(midpoints or barycenter) will become a heavy burden.

2.1.2 Human model

Many kinds of human models with complex issue structures and detailed body profile have been developed[38, 39] for the studies on biological effects of human exposure. Anyhow, since the main target of this work is to evaluate the accuracy of the proposed procedure on estimating the internal electric field, a 3D version of homogeneous human model indicated by international standards related to the human exposure to low-frequency electric fields, magnetic fields and electromagnetic fields has been adopted. The 2D version has been applied to the investigation of the upper bound of the exposure (reference levels of induced electric field)[40].

The male model with electrical conductivity σ=0.2 S/m and relative electrical permittivity $\varepsilon_r = 10^5$ in compliance with the standard has been chosen and its profile is shown in Figure. 2.2. It is symmetric about the central axis with about 1400 discretized meshes (triangular elements) over the body surface.

2.2 EFIE and MFIE

The principle of the numerical approach is derived from Electric Field Integral Equation (EFIE) and Magnetic Field Integral Equation (MFIE), which are deduced from

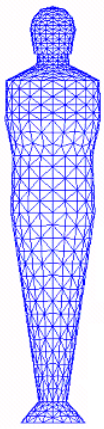

Figure 2.2: 3D human body model

Maxwell's equations. In sinusoidal steady state, Maxwell's equations can be expressed as

$$\nabla \times \hat{\mathbf{E}} = -j\omega\hat{\mathbf{B}} \tag{2.1}$$

$$\nabla \times \hat{\mathbf{H}} = \hat{\mathbf{J}} + j\omega\hat{\mathbf{D}} \tag{2.2}$$

$$\nabla \cdot \hat{\mathbf{B}} = 0 \tag{2.3}$$

$$\nabla \cdot \hat{\mathbf{D}} = \hat{\rho} \tag{2.4}$$

where j is imaginary unit, ω represents angular frequency and $\hat{\rho}$ refers to complex form of charge density. If the medium which the equations are applied in is linear, homogeneous and isotropic with electric permittivity ε, magnetic permeability μ and electrical conductivity σ, Eq.2.1 to Eq.2.4 becomes:

$$\nabla \times \hat{\mathbf{E}} = -j\omega\mu\hat{\mathbf{H}} \tag{2.5}$$

$$\nabla \times \hat{\mathbf{H}} = \hat{\mathbf{J}} + (\sigma + j\omega\varepsilon)\hat{\mathbf{E}} \tag{2.6}$$

$$\nabla \cdot \hat{\mathbf{H}} = 0 \tag{2.7}$$

$$\nabla \cdot \hat{\mathbf{E}} = \hat{\rho}/\varepsilon \tag{2.8}$$

based on relations $\hat{\mathbf{D}} = \varepsilon\hat{\mathbf{E}}$ and $\hat{\mathbf{B}} = \mu\hat{\mathbf{H}}$. As a matter of fact, Eq. 2.5 to Eq. 2.8 are still valid even if the field vector is non-sinusoidal, since it can be always treated as a superposition of various frequency components according to Fourier transform.

Taking the curl of Eq. 2.5 and substituting on the left side of Eq. 2.6, the electric field $\hat{\mathbf{E}}$ can be obtained without getting magnetic field $\hat{\mathbf{H}}$ involved as in Eq. 2.9:

$$\nabla \times \nabla \times \hat{\mathbf{E}} = \omega^2\mu(\varepsilon - j\frac{\sigma}{\omega})\hat{\mathbf{E}} - j\omega\mu\hat{\mathbf{J}} = \hat{k}^2\hat{\mathbf{E}} - j\omega\mu\hat{\mathbf{J}} \tag{2.9}$$

In a similar way, $\hat{\mathbf{H}}$ can be expressed without terms of $\hat{\mathbf{E}}$ as in Eq. 2.10:

$$\nabla \times \nabla \times \hat{\mathbf{H}} = \omega^2\mu(\varepsilon - j\frac{\sigma}{\omega})\hat{\mathbf{H}} + \nabla \times \hat{\mathbf{J}} = \hat{k}^2\hat{\mathbf{H}} + \nabla \times \hat{\mathbf{J}} \tag{2.10}$$

where $\hat{k} = \omega\sqrt{\mu(\varepsilon - j\frac{\sigma}{\omega})}$is the propagation coefficient in frequency domain.

In order to solve Eq. 2.9, a Green function must be introduced:

$$\hat{\mathbf{G}} = \frac{e^{-j\hat{k}R}}{R}\mathbf{a} = \hat{\Psi}\mathbf{a} \tag{2.11}$$

where $\mathbf{a}$ is an arbitrary constant unit, and $R = |\mathbf{r} - \mathbf{r}'|$ is the distance between any point in space P and an electromagnetic source point Q.

Green function is one of the fundamental tools in Mathematics and Physics. It can be configured to various forms in order to solve different problems, such as Poisson's or Laplace's Equation in electrostatic fields and Helmholtz equation in time-varying fields. Normally, it is the solution of a point source with simple boundary conditions, which combined together with more complex field problems through Green identities. In fact, $\hat{\Psi}$ in Eq. 2.11 is one of the solutions of the complex Helmholtz equation.

Make use of *Vector Green's Theorem* (Eq. 8.6) to combine vector Green function $\hat{\mathbf{G}}$ and electric field $\hat{\mathbf{E}}$ together, one may receive:

$$\int_\Omega (\hat{\mathbf{E}} \cdot \nabla \times \nabla \times \hat{\Psi}\mathbf{a} - \hat{\Psi}\mathbf{a} \cdot \nabla \times \nabla \times \hat{\mathbf{E}})dv = -\oint_{\partial\Omega} (\hat{\Psi}\mathbf{a} \times \nabla \times \hat{\mathbf{E}} - \hat{\mathbf{E}} \times \nabla \times \hat{\Psi}\mathbf{a}) \cdot \mathbf{n}ds \tag{2.12}$$

The problem introduced by Green function is the singularity of the point source, i.e. when $R = 0$. The solution is to exclude a smaller sphere $\partial\Omega_0$ (with radius $\zeta \to 0$) that

includes P inside boundary surface $\partial\Omega$ (half sphere applied when P locates over $\partial\Omega$, and then Eq. 2.12 becomes:

$$\int_{\Omega-\Omega_0}(\hat{\mathbf{E}}\cdot\nabla\times\nabla\times\hat{\Psi}\mathbf{a}-\hat{\Psi}\mathbf{a}\cdot\nabla\times\nabla\times\hat{\mathbf{E}})dv=-\oint_{\partial\Omega}(\hat{\Psi}\mathbf{a}\times\nabla\times\hat{\mathbf{E}}-\hat{\mathbf{E}}\times\nabla\times\hat{\Psi}\mathbf{a})\cdot\mathbf{n}ds \\ -\oint_{\partial\Omega_0}(\hat{\Psi}\mathbf{a}\times\nabla\times\hat{\mathbf{E}}-\hat{\mathbf{E}}\times\nabla\times\hat{\Psi}\mathbf{a})\cdot\mathbf{n}ds \tag{2.13}$$

where the normal unit vector $\mathbf{n}$ directs towards Ω.

By applying Eq. 2.9 on the left of Eq. 2.13, finally the electric field at any Point P can be obtained through Eq. 2.14.

$$\hat{\mathbf{E}}(P)=\frac{1}{4\pi}\int_{\Omega}(\frac{\hat{\rho}}{\varepsilon}\nabla\hat{\Psi}-j\omega\mu\hat{\Psi}\hat{\mathbf{J}}_{\mathbf{s}})dv+\frac{1}{4\pi}\oint_{\partial\Omega}[(\mathbf{n}\cdot\hat{\mathbf{E}})\nabla\hat{\Psi}+(\mathbf{n}\times\hat{\mathbf{E}})\times\nabla\hat{\Psi}-j\omega\mu\hat{\Psi}(\mathbf{n}\times\hat{\mathbf{H}})]ds \tag{2.14}$$

The magnetic field at point P can be deduced from a similar procedure

$$\hat{\mathbf{H}}(P)=\frac{1}{4\pi}\int_{\Omega}(\hat{\mathbf{J}}_{\mathbf{s}}\times\nabla\hat{\Psi})dv+\frac{1}{4\pi}\oint_{\partial\Omega}[j\omega(\varepsilon-j\frac{\sigma}{\omega})\hat{\Psi}(\mathbf{n}\times\hat{\mathbf{E}})+(\mathbf{n}\times\hat{\mathbf{H}})\times\nabla\hat{\Psi}+(\mathbf{n}\cdot\hat{\mathbf{H}})\nabla\hat{\Psi}]ds \tag{2.15}$$

In Eq. 2.14 and Eq. 2.15, the volume integrals for both equations include the all the sources that producing electromagnetic fields (free charges and currents), while surface integrals represent the contribution of the equivalent sources over such surface. Since the charge density $\hat{\rho}$ can be replaced by a term related to the divergence of $\hat{\mathbf{J}}_{\mathbf{s}}$ through the continuity equation Eq. 2.16[41], it is possible to present the sources in Eq. 2.14 only in terms of the electric current $\hat{\mathbf{J}}_{\mathbf{s}}$.

$$\nabla\cdot\hat{\mathbf{J}}=-j\omega\hat{\rho} \tag{2.16}$$

The discretization process of BEM approximation is carried out over the surface $\partial\Omega$, by assuming that the surface is divided into M triangular elements and on the m-th element, the electric and magnetic field are uniform. The radiation sources are contained within the sub-domain Ω_s. Then Eq. 2.14 and Eq. 2.15 become

$$\xi\hat{\mathbf{E}}(P)=-j\omega\mu\int_{\Omega_s}\hat{\Psi}\hat{\mathbf{J}}_{\mathbf{s}}dv+\sum_{m=1}^{M}\oint_{\partial\Omega_m}(\mathbf{n}_m\cdot\hat{\mathbf{E}}_m)\nabla\hat{\Psi}_m ds+\sum_{m=1}^{M}(\mathbf{n}_m\times\hat{\mathbf{E}}_m)\times\oint_{\partial\Omega_m}\nabla\hat{\Psi}_m ds \\ -j\omega\mu\sum_{m=1}^{M}(\mathbf{n}_m\times\hat{\mathbf{H}}_m)\oint_{\partial\Omega_m}\hat{\Psi}_m ds \tag{2.17}$$

$$\xi\hat{\mathbf{H}}(P) = \int_{\Omega_s}(\hat{\mathbf{J}}_\mathbf{s}\times\nabla\hat{\Psi})dv + \sum_{m=1}^{M}(\mathbf{n}_m\cdot\hat{\mathbf{H}}_m)\oint_{\partial\Omega_m}\nabla\hat{\Psi}_m ds + \sum_{m=1}^{M}(\mathbf{n}_m\times\hat{\mathbf{H}}_m)\times\oint_{\partial\Omega_m}\nabla\hat{\Psi}_m ds$$
$$+j\omega(\varepsilon - j\frac{\sigma}{\omega})\sum_{m=1}^{M}(\mathbf{n}_m\times\hat{\mathbf{E}}_m)\oint_{\partial\Omega_m}\hat{\Psi}_m ds \tag{2.18}$$

Here the singularity factor $\xi = \frac{1}{2}$ if P locates on the surface $\partial\Omega$, otherwise $\xi = 1$. Eq. 2.17 and Eq. 2.18 are discretized forms of EFIE and MFIE[42].

2.3 Electromagnetic Field reconstruction

If Point P exists inside a source-free region Ω, according to Eq. 2.14 and Eq. 2.15, the electromagnetic field distribution of this region depends on the equivalent sources on Surface $\partial\Omega$. Therefore, they can be applied in free space field computation, under the assumption that no electromagnetic sources are presented in the same region as Point P (Eq. 2.19 and Eq. 2.20).

$$\hat{\mathbf{E}}(P) = \frac{1}{4\pi}[-\oint_{\partial\Omega}(\mathbf{n}\times\hat{\mathbf{E}})\times\nabla\hat{\Psi}ds - \oint_{\partial\Omega}(\mathbf{n}\cdot\hat{\mathbf{E}})\nabla\hat{\Psi}ds + j\omega\mu\oint_{\partial\Omega}\hat{\Psi}(\mathbf{n}\times\hat{\mathbf{H}})]ds \tag{2.19}$$

$$\hat{\mathbf{H}}(P) = \frac{1}{4\pi}[-\oint_{\partial\Omega}(\mathbf{n}\times\hat{\mathbf{H}})\times\nabla\hat{\Psi}ds - \oint_{\partial\Omega}(\mathbf{n}\cdot\hat{\mathbf{H}})\nabla\hat{\Psi}ds - \oint_{\partial\Omega}(\sigma + j\omega\varepsilon)\hat{\Psi}(\mathbf{n}\times\hat{\mathbf{E}})ds] \tag{2.20}$$

where $\mathbf{n}$ directs inward the surface $\partial\Omega$. μ refers to vacuum permeability μ_0, and the equivalent electrical conductivity ε includes all losses.

In order to compute the fields in free space, both the normal and two tangential components of the electric and magnetic field must be known. Therefore, totally 6 scalar equations (3 for electric field and 3 for magnetic field) can be derived from the two vector equations Eq. 2.19 and Eq. 2.20.

The corresponding discretized forms are given in Eq. 2.21 and Eq. 2.22,

$$\hat{\mathbf{E}}(P) = -\sum_{i=1}^{N}[(\mathbf{n}_i\times\hat{\mathbf{E}}_i)\times\oint_{\partial\Omega_i}\nabla\hat{\Psi}ds + (\mathbf{n}_i\cdot\hat{\mathbf{E}}_i)\oint_{\partial\Omega_i}\nabla\hat{\Psi}ds] + j\omega\mu\sum_{i=1}^{N}[(\mathbf{n}_i\times\hat{\mathbf{H}}_i)\oint_{\partial\Omega_i}\hat{\Psi}ds] \tag{2.21}$$

$$\hat{\mathbf{H}}(P) = -\sum_{i=1}^{N}[(\mathbf{n}_i \times \hat{\mathbf{H}}_i)\oint_{\partial\Omega_i} \times \nabla\hat{\Psi}ds + (\mathbf{n}_i \cdot \hat{\mathbf{H}}_i)\oint_{\partial\Omega_i} \nabla\hat{\Psi}ds] - (\sigma + j\omega\varepsilon)\sum_{i=1}^{N}[(\mathbf{n}_i \times \hat{\mathbf{E}}_i)\oint_{\partial\Omega_i} \hat{\Psi}ds] \tag{2.22}$$

where $\partial\Omega_i$ denotes the *i-th* elementary triangular. The surface $\partial\Omega$ is divided into N elements. On each of them, both the phases and amplitudes must be known to configure the complex electric and magnetic field. Besides the normal and tangential components depend on the local coordinate of the elements. Apparently, a regular shape of the surface (such as parallelepiped and sphere) would significantly simplify the experimental procedure.

Fortunately, it can be arbitrarily chosen as long as all the sources are included in. Kronrod's algorithm is applied for the numerical computation of the integration of Green's function $\hat{\Psi}$ as well as its gradient $\nabla\hat{\Psi}$ on each discretized surface $\partial\Omega_i$.

Now, the fields reconstruction procedure in free space has been built up, requiring only the knowledge of fields over a discretized surface which encloses all the electromagnetic sources. The number of the discretized elements corresponds with the necessary field vectors on the boundary. Another advantage of this procedure is that, there is no specified requirement on the type of sources contained inside the surface. However, when ferromagnetic materials are present in the source, a Fourier transformation must be applied in order to decompose the fields to obtain the field contribution for each harmonic component, following Eq. 2.21 and Eq. 2.22. The total fields at any point outside the boundary surface is the superposition of all these field contribution.

2.4 Magnetic field reconstruction in low frequency

At low frequency range ($\leq$100 kHz), the computational procedure of the fields in free space (ε_0 and μ_0 are set as in vacuum) can be simplified taken into account following facts:

- the propagation coefficient ($k = \frac{2\pi}{\lambda}$) is relatively small since the wavelength $\lambda \geq 3 \times 10^3$ m and the coupling between the electric field and magnetic field almost doesn't exist;
- the energy of the electric field is negligible.

Out of these considerations, the discretized form of magnetic field distribution (Eq. 2.23) can be derived directly from Eq. 2.22:

$$\mathbf{H}(P) = \sum_{i=1}^{N} (\mathbf{n}_i \times \mathbf{H}_i) \times \oint_{\partial\Omega_i} \nabla\Psi ds + \sum_{i=1}^{N} (\mathbf{n}_i \cdot \mathbf{H})_i \oint_{\partial\Omega_i} \nabla\Psi ds \tag{2.23}$$

Here the point source solution for wave equations becomes

$$\Psi = \frac{1}{4\pi R} \tag{2.24}$$

Eq. 2.24 is the suitable Green function applied to solve magnetic field problem in Eq. 2.23.

Eq. 2.23 states that the magnetic field in the free space can be deduced from only the knowledge of **H** on an arbitrary surface enclosing all the sources. Of course **H** is defined by three components of a Cartesian reference frame and, under sinusoidal operating conditions, each component is in general associated to a complex number with both real and imaginary part.

2.5 Induced electric field Estimation

The fields at any point P inside the human model can be obtained through the same approximation procedure of BEM described in Eq. 2.21 and Eq. 2.22, if the field distribution over the internal surface of the body are known. However, in practice it is almost impossible to obtain the fields directly inside the body. Thanks to the continuity conditions in Eq. 2.25, they can be substituted with the external field vectors.

$$\begin{gathered} \hat{E}_{\tau_1}^{(a)} = -\hat{E}_{\tau_1}^{(b)}, \quad \hat{E}_{\tau_2}^{(a)} = \hat{E}_{\tau_2}^{(b)}, \quad \hat{E}_n^{(a)}(\sigma + j\omega\varepsilon)^{(a)} = -\hat{E}_n^{(b)}(\sigma + j\omega\varepsilon)^{(b)} \\ \hat{H}_{\tau_1}^{(a)} = -\hat{H}_{\tau_1}^{(b)}, \quad \hat{H}_{\tau_2}^{(a)} = \hat{H}_{\tau_2}^{(b)}, \quad \hat{H}_n^{(a)}\mu^{(a)} = -\hat{H}_n^{(b)}\mu^{(b)} \end{gathered} \tag{2.25}$$

where superscribe a and b refer to out in free space and inside human model respectively. It means it is possible to estimate the induced fields inside the human body in a non-invasive way through the proposed BEM procedure.

In low frequency range, since the induced currents inside human body caused by the applied magnetic field do not perturb the environmental fields, the magnetic fields over the external body surface can be provided by the reconstruction procedure based on Eq. 2.23. Moreover, taken into account that the conduction current densities are always

prevailing with respect to the dielectric ones at low frequency, the normal component of electric field should not exist on the boundary.

So finally, the electric field at any point P inside the model can be calculated following Eq. 2.26:

$$\mathbf{E}(P) = -\sum_{i=1}^{I}[(\mathbf{n}_i \times \mathbf{E}_i) \times \oint_{\partial\Omega_i} \nabla\Psi ds] + j\omega\mu \sum_{i=1}^{I}[(\mathbf{n}_i \times \mathbf{H}_i) \oint_{\partial\Omega_i} \Psi ds] \tag{2.26}$$

where I is the number of discretized elements over the body surface and the unit normal vector $\mathbf{n}$ directs inward the surface. The electric fields at any Point P is a summation of all the electric field and magnetic field contributions of the surface elements. According to Eq. 2.26, the electric field on the barycenter of each triangular elements over the discretized internal body surface must be known in advance.

Making use of the known internal magnetic field distribution (coming from the magnetic field reconstruction), the electric fields on the $j\text{-}th$ element $\mathbf{E}_j$ can be expressed as Eq. 2.27:

$$\xi\mathbf{E}_j = -\sum_{i=1}^{I}[(\mathbf{n}_i \times \mathbf{E}_i) \times \oint_{\partial\Omega_i} \nabla\Psi ds] + j\omega\mu \sum_{i=1}^{I}[(\mathbf{n}_i \times \mathbf{H}_i) \oint_{\partial\Omega_i} \Psi ds] \tag{2.27}$$

The electric field problems over the internal surface can be solved by imposing $\frac{1}{2}$ to ξ. Eq.2.27 is derived directly from 2.17 (in source free region), by applying low frequency simplification.

The proposed field solution can be also applied to the investigation of the induced field distribution of complex human models with more tissues, as long as the electromagnetic parameters of all tissues are given. In this case, both the body surface and all the boundaries of the tissues must be taken into account for the surface integral.

3

Simulations on Helmholtz coils system

3.1 Introduction

The proposed hybrid procedure aiming to reconstruct the field distributions produced by unknown electric and magnetic sources has been well explained in the last chapter. Before proceeding to the experimental verifications, a study based on simulation is taken out as a preliminary validation step.

There are several important aspects for this simulative procedure in the hybrid field reconstruction method.

Firstly it gives a general idea on the number of measurement points which is necessary to well reconstruct the field distributions. In the meanwhile, it provides a quantitative evaluation of the discrepancy which comes only from the numerical computation. Moreover, it helps to develop the numerical fitting method specified in the last section which could significantly simplify the experiments.

During this study, the actual measurement data will be substituted with 'virtual' one provided by simulation. The investigation on the field reconstruction quality will be carried out through the comparison between the predictions from BEM procedure and computational results of different electric and magnetic sources, together with the analysis of the error distributions.

3.2 Helmholtz model

In order to evaluate the performance of this field reconstruction procedure around 'unknown sources', some well 'known sources' must be presented, as the reference for the generating field. At the same time, these sources are able to provide the computational values on the 'virtual' measurement points over the virtual surface.

As the magnetic sources at low frequency range (up to 100 kHz), the Helmholtz system has been chosen. The coils have 17 turns for each, with diameter of 700 mm, while the thickness along the main axis (z axis) is 65 mm, as indicated in Figure 3.1a (the thickness along the radius is 1 mm). The archetype of this model, the 'reference magnetic fields generation system' built up by Istituto Nazionale di Ricerca Metrologica (I.N.RI.M.), is shown in Figure 3.1b. There will be a specific introduction about this system in the following chapter.

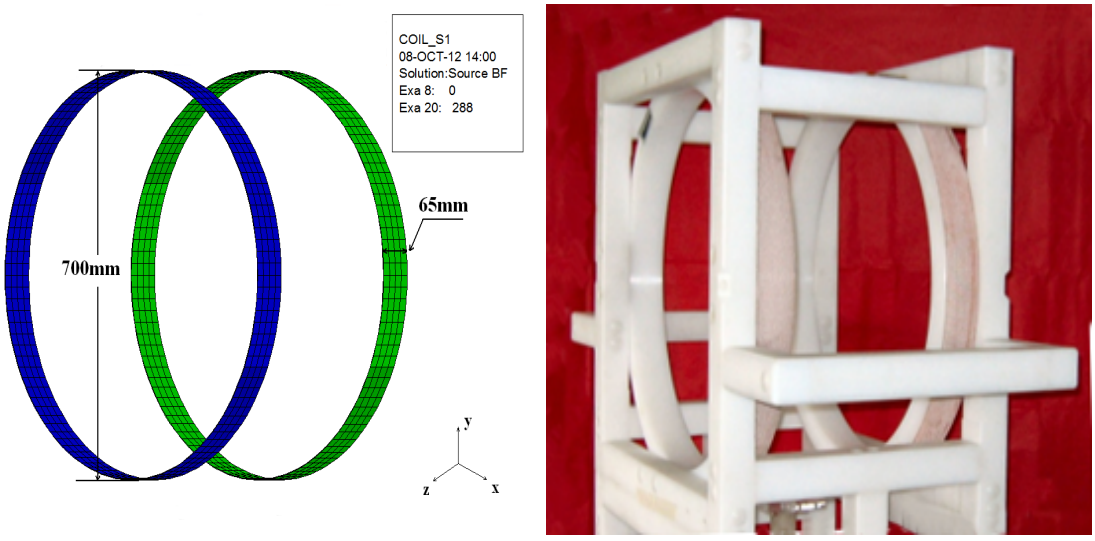

(a) Helmholtz coils model **(b)** Reference magnetic fields generation system

Figure 3.1: Helmholtz coils system

The two coils are divided into 288 volumes in the model. The magnetic field at any point in free space is the superimposition for each element based on Biot-Savart law [43].

Three types of magnetic field distributions will be generated from this system, by separately controlling the supply currents flowing in each coil (this can be realized by

the reference field generation system shown in Figure 3.1b as well). The amplitudes of the currents flowing in both of the coils are equal, while the phases are arranged to be various. Figure 3.2 demonstrates the three different arrangements of the phases in complex plan.

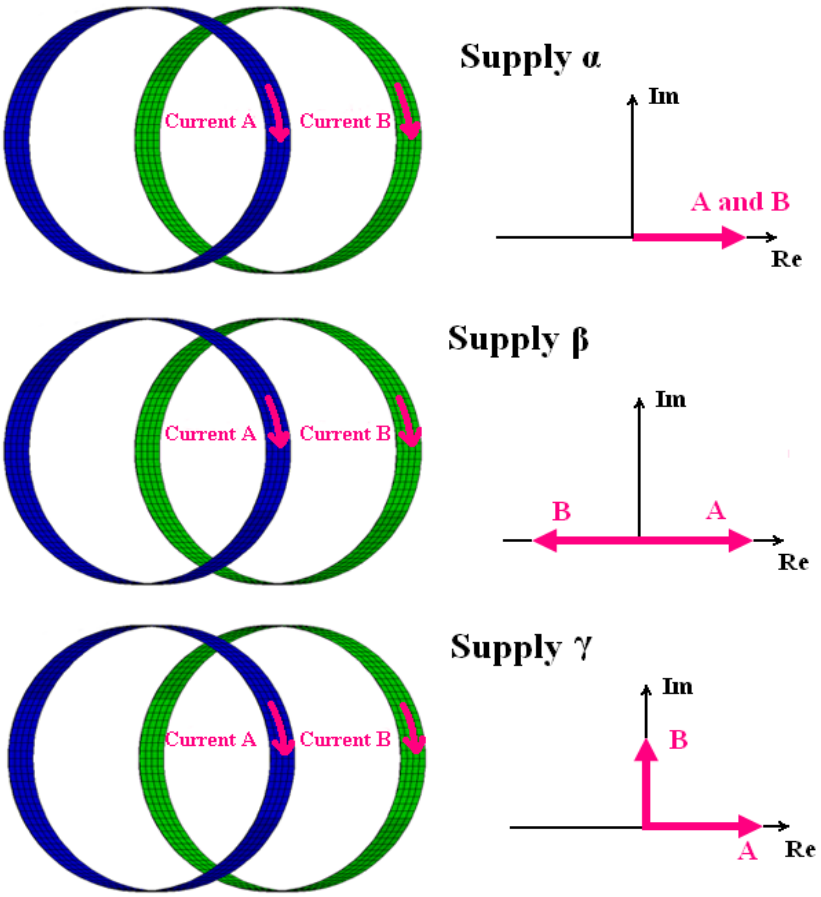

Figure 3.2: Supply conditions

In the figure, Supply α represents that the currents A and B flowing in the two coils have the same phases, which means the two coils are serially connected. Outside the Helmholtz system where the field distributions of the two coils are strongly interacted on each other, the resultant fields direct to the main axis of the system (z axis). Under Supply β where currents A and B are in opposite direction, high field gradients can be found at the same region due to the radial field fluxes generated from both of the coils (take reference in the last chapter). With Supply γ, the Current B has a 90 ° shift from

Current A. As a result, all the fields around the system are no longer in phase. To sum up, each supply condition represents a unique distribution of magnetic field.

3.3 Results and discussions

As a fundamental step for the BEM reconstruction procedure, a virtual surface must be selected to enclose all the electromagnetic sources. Theoretically, the shape and dimension of this surface can be arbitrary. However, a regular shape (a cylinder or parallelepiped) should be considered as in practical work since it makes easier the positioning of the probe during practical measurements. In the meanwhile, the surface should keep distance from the sources in order to avoid strong gradients of the fields where the accuracy of the measurement would be influenced significantly. A 720 mm× 720 mm× 540 mm parallelepiped which has the same center as the Helmholtz system has been applied in this simulation (as shown in Figure 3.3a).

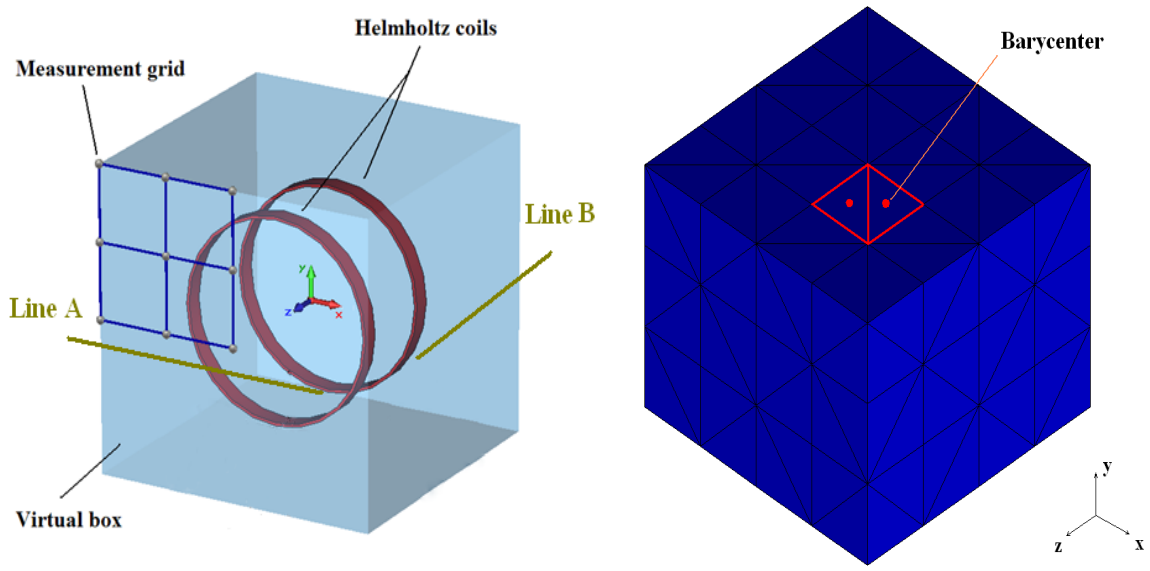

(a) Scheme of closed surface around Helmholtz system

(b) Discretized surface for BEM reconstruction

Figure 3.3: BEM modeling procedure

Once the parameters has been fixed, the surface will be discretized into triangular elements as discussed in the last chapter through MSC.Patran [44]. The magnetic field

on each triangle is assumed to be uniform, represented by the field vector located at the barycenter as demonstrated in Figure 3.3b.

Different amount of discretized triangular elements are applied to this surface, and ten investigation points are chosen outside the discretized surface, in order to evaluate the accuracy of the proposed reconstruction method, through the relative local error specified in Eq. 3.1.

$$\eta = \frac{\sqrt{\sum_{k=1}^{3}[(H_{k,r}^{S} - H_{k,r}^{R})^2 + (H_{k,i}^{S} - H_{k,i}^{R})^2]}}{\sqrt{\sum_{k=1}^{3}[(H_{k,r}^{S})^2 + (H_{k,i}^{S})^2]}} \tag{3.1}$$

The subscript k refers to the three components (x, y and z), while the other two refers to real (r) and imaginary (i) part of the field vector. The superscripts S and R represent reference (Biot-Savart) and BEM reconstruction respectively.

Position (m)	**1**	**2**	**3**	**4**	**5**	**6**	**7**	**8**	**9**	**10**
x	0.2	0.4	0.0	0.4	0.0	1.08	1.08	1.08	1.08	1.08
y	0.2	0.4	0.4	0.0	0.0	0.2	0.4	0.0	0.4	0.0
z	1.08	1.08	1.08	1.08	1.08	0.2	0.4	0.4	0.0	0.0

Table 3.1: Positions of the investigation points

Table 3.1 lists the investigation points which spread on two planes (xy plane and yz plane) about 0.75 m away from the surface. The evaluation of the accuracy on these ten points should give a preview on the quality of this reconstruction procedure because the field distributions of the whole system is cylindrically symmetric about z axis.

The magnetic field values on these points and the relative local error under Supply α and Supply β are shown in Figure 3.4. The supply current is about 1 A for each coil.

Under the Supply α, the first five points located at the front of one coil have relatively higher magnetic fields than the other five on the lateral part of the two coils. For most of the points, the error drops significantly with the increasing number of discretized elements used in the reconstruction, although reversal examples appear in some critical locations where the field values are higher than 2 A/m (point 5) or lower than 1 A/m (point 8 to 10). No doubt that a satisfactory field reconstruction requires more than 100 elements.

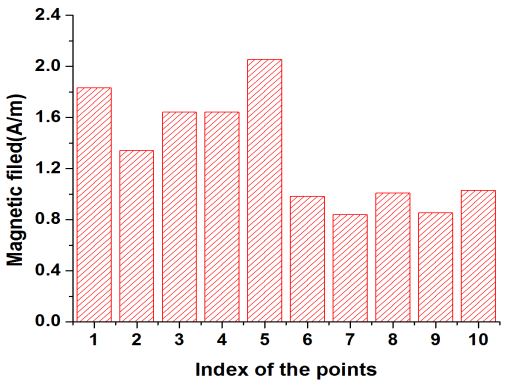

(a) Magnetic field values with Supply α

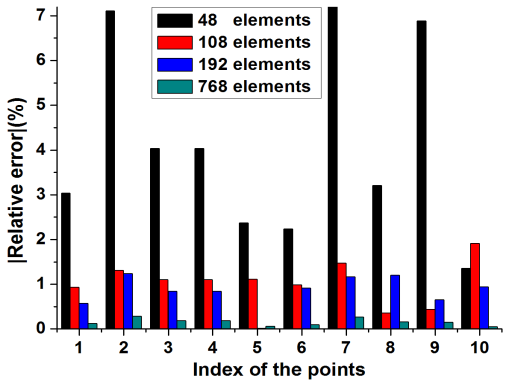

(b) Relative local error in percent

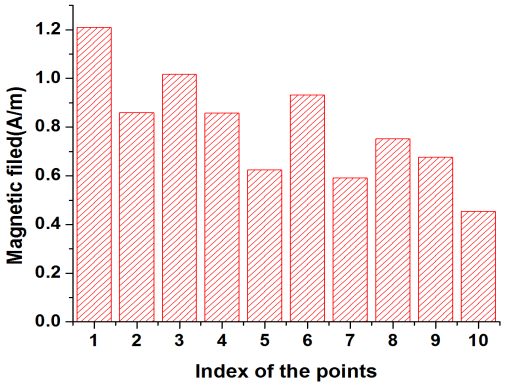

(c) Magnetic field values with Supply β

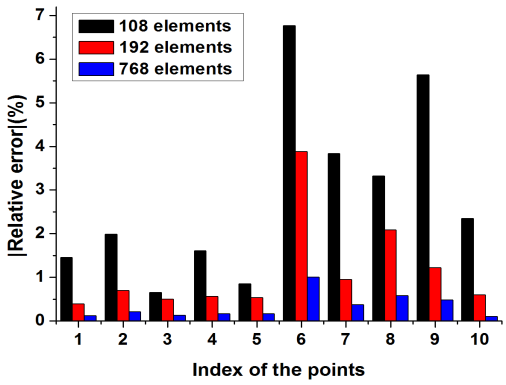

(d) Relative local error in percent

Figure 3.4: Magnetic field reconstructions with Supply α and β

The results under Supply β with the same evaluation procedure are shown in Figure 3.4c and 3.4d. From the previous discussion about the supply conditions, one may conclude that Supply β and γ have more complicated field distributions than Supply α. Therefore in Figure 3.4d, the results coming from 48 elements have been eliminated.

In general, with Supply β the field level is lower compared with Supply α. The errors of reconstruction increase mainly in the last five points where higher field gradients exist. The largest disagreement between Biot-Savart and BEM Reconstruction appears at point 6, which is closer to the coil. It may due to the fact that during the approximation of BEM some critical points where field vectors have sharp turn are missing. In any case, with higher number of discretized elements (768), the errors can be limited to 1% or below.

According to the error evaluation above, more than 192 elements should be applied to the BEM procedure to well reconstruct the field distributions produced by first two supply conditions. More investigation has been carried out on two horizontal lines focusing on 192 elements and 768 elements for all three kinds of supplies. The positions of the investigation lines are indicated in Figure 3.3a, where Line A starting from point (-0.52, 0, 1.01) to point (0.52, 0, 1.01), while Line B from (1.01, 0, 0.52) to (1.01, 0, -0.52).

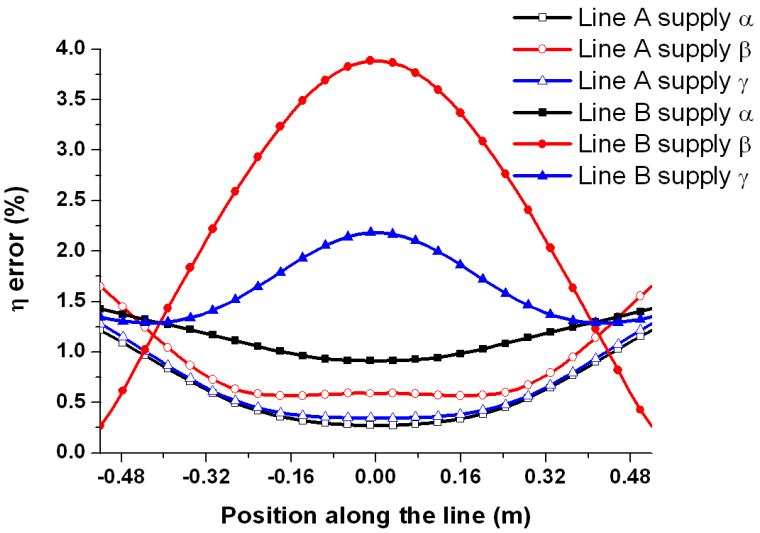

Figure 3.5: Distribution of error η (in percent) along lines A and B for the three different supply conditions (reconstructed from 192 elements)

Figure 3.5 stresses that the worst accuracy comes always from Line B, when the virtual surface is discretized into 192 elements. The relative error reaches 4% in the center of the line under Supply β, where the field is weakest among all the considered three supplies. On the contrary, for Line A, the error distribution lines are close to each other, because the field generated in front of the coils are almost the same (only difference could be the field strength or slight phase shift). Supply γ has medium error behavior in both lines, because the field level concerned both the gradient and the strength is between the other two supply conditions.

The error distributions while using 768 elements for reconstruction are similar to the previous ones, although the relative error drops below 1% (below 0.5 % except Line B under Supply β), which means great agreements between proposed BEM procedure and

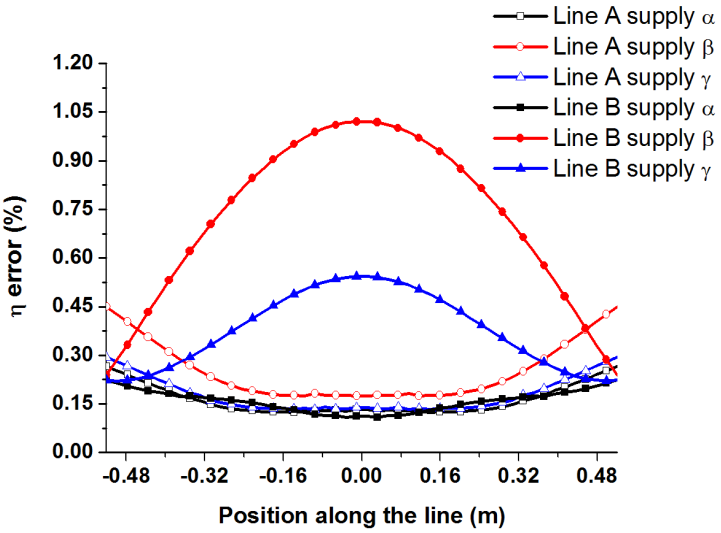

Figure 3.6: Distribution of error η (in percent) along lines A and B for the three different supply conditions (reconstructed from 768 elements)

computational results from Biot-Savart. The relatively high discrepancy still happens at Line B, when the supply currents are not in the same direction (regarding to Figure 3.2).

3.4 Interpolation/Extrapolation method

The reliability of this reconstruction procedure has been verified in the last section. However, there may exist some problems on practical utility. The major one is the large requirement of measurements . A possible way to solve it could be the application of automatic positioning system. However, this may lead to another problem in the difficulties of the design of such positioning system, since the specific location (i.e. the barycenter of the triangular elements shown in Figure 3.3b) is required for each measurement. The consequence of a tiny error in the positioning could be severe when passing through the computational procedure of the reconstruction.

Given consideration of the complication mentioned above, an interpolation/ extrapolation method has been introduced, taking reference from [45].

Suppose there are a set of data points which consist of a position vector $\boldsymbol{x}$(independent variables including x, y and z for each) and one of three components of the field vector v (the dependent variable), denoted by $\{\boldsymbol{x}^{(i)}, v^{(i)}\}_{i=1}^{n}$, where n is the number of input

points. The output scalar G (i.e. one of the field components corresponding to the barycenter of triangular elements), is a linear combination demonstrated by Eq. 3.2.

$$G = \sum_{i=1}^{m} w^{(i)} g^{(i)} \tag{3.2}$$

This weighted network associate with a set of unknown weights $\{w^{(i)}\}_{i=1}^{m}$ and a set of radial basis functions $\{g^{(i)}\}_{i=1}^{m}$, where $m \leq n$. Reference [45] provides some common choices for g_i. Two of them listed below might be suitable in this application.

- Inverse multiquadrics (IM)
  $g^{(i)} = \frac{a}{\sqrt{r^2+a^2}}$ for some $a > 0$
- Gaussians (GA)
  $g^{(i)} = exp(-\frac{r}{2a})$ for some $a > 0$

with $r = \|\boldsymbol{x} - \boldsymbol{c}^{(i)}\|$, where $\|\cdot\|$ denotes the Euclidean norm and $\{\boldsymbol{c}^{(i)}\}_{i=1}^{m}$ is a set of the centers that can be chosen from among the input points or position vectors of the output. The unknown weights $\{w^{(i)}\}_{i=1}^{m}$ can be found by $\boldsymbol{G}\boldsymbol{w} = \boldsymbol{y}$, where $\boldsymbol{w} = [w^{(1)}, w^{(2)}, ..., w^{(m)}]^T$, $\boldsymbol{y} = [y^{(1)}, y^{(2)}, ..., y^{(m)}]^T$, $G = \begin{bmatrix} g^{(1)}(\boldsymbol{x}^{(1)}) & g^{(2)}(\boldsymbol{x}^{(1)}) & \cdots & g^{(m)}(\boldsymbol{x}^{(1)}) \\ g^{(1)}(\boldsymbol{x}^{(2)}) & g^{(2)}(\boldsymbol{x}^{(2)}) & \cdots & g^{(m)}(\boldsymbol{x}^{(2)}) \\ \vdots & \vdots & \ddots & \vdots \\ g^{(1)}(\boldsymbol{x}^{(n)}) & g^{(2)}(\boldsymbol{x}^{(n)}) & \cdots & g^{(m)}(\boldsymbol{x}^{(n)}) \end{bmatrix}$, under the special case where n=m.

The parameter a is obtained from $a = r_{max}/2n$, although it could be tunable to adjust specified procedure, by multiplying a suitable coefficient. Table 3.2 lists the average errors along Line B with different coefficients for parameter a. Enlarge this parameter may have opposite effects with different field distribution conditions according to the table. For smooth, uniform fields, relatively small coefficient could fit better while large one will do for high gradients.

	$2a$	$2.5a$	$3a$	$3.5a$	$4a$
Supply α	0.372	0.383	0.605	0.788	0.931
Supply β	2.02	1.72	1.57	1.51	1.50

Table 3.2: Average errors with different coefficients (in percent)

The accuracy of the reconstruction through these two basis functions has been tested along Line B under supply condition β as shown in Figure 3.7. Two sets of input data (n=98 and n=192) have been applied separately in order to receive an output of field vectors on 768 points which located in the barycenter of all the discretized elements on the surface.

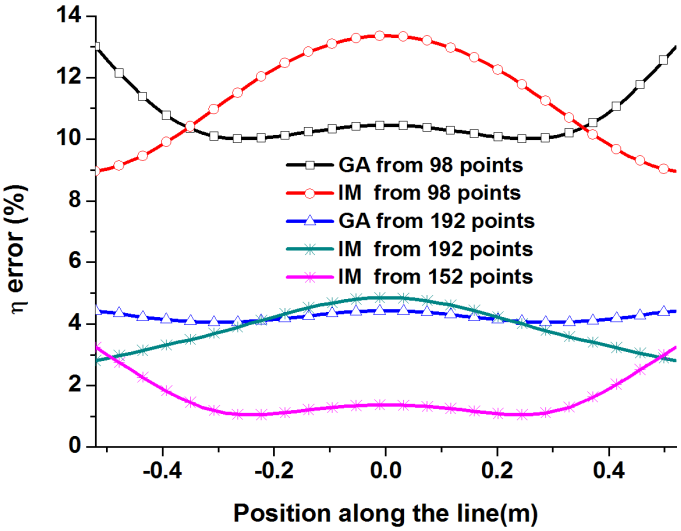

Figure 3.7: Distribution of error η (in percent) along Line B with different number of points for interpolation/extrapolation

The error distributions from different basis functions are of the same order of magnitude with same number of input data. Clearly more points used as input, better accuracy could be obtained. However, the inverse multiquadrics has been chosen in the reconstruction procedure. Through the comparison of the trend of the distribution lines in Figure 3.7, it is obvious that the errors from IM are turning down at both ends of the line, which means due to the convergent property of the structure IM function has more stable behavior at extrapolation area.

The last set of input (n=152) comes from a regular grid over the surface as indicated in Figure 3.3a, so that the extrapolation can be avoided since a number of points on the edges has been included. The error distribution from this set of data shows the best accuracy among all the input, even if the number of input is lower than 192. The arrangement of the positions of the input points has an influence on the interpolation/ extrapolation results.

4

Experimental validations

4.1 Introduction

As a hybrid procedure, experimental performance is essential to its practical application. This chapter will elaborate the experimental method for this procedure and discuss the field reconstruction results starting from the measurements.

Various field distributions around the archetype of the Helmholtz coils system mentioned in the previous chapter(Figure 3.1b) will be generated. The measurement will be performed on a regular grid and then used as input for the BEM procedure, after making use of the interpolation/extrapolation method well developed in section 3.4 and the symmetric feature of the field distributions generated from Helmholtz coils. Since the model in the last chapter was built making reference to the Helmoltz coil generation system, the reconstruction results can be brought to comparison not only with the direct measurements in free space, but also with the simulation.

4.1.1 Reference field generation system (up to 100 kHz)

The Helmholtz system is developed to generate the reference magnetic fields at low and intermediate frequency in Istituto Nazionale di Ricerca Metrologica (I.N.RI.M.). This system is mainly used for the traceable calibration of magnetic field meter (as illustrated in Figure 4.1a).

The value of the magnetic flux density generated in the system center is up to 100 μT at 1 kHz and 25 μT at 100 kHz with a maximum supply current of 2.2 A. The Helmholtz coils system is characterized as following [46]:

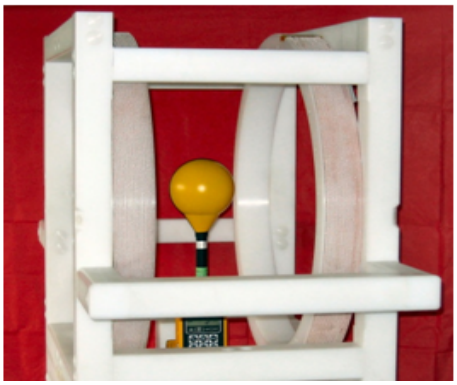

(a) Helmholtz system with a meter under test

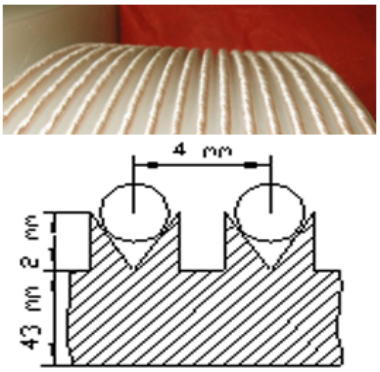

(b) Litz wires and the support arrangement

Figure 4.1: INRIM Helmholtz coil system for the generation of reference magnetic fields up to 100 kHz.

- Circular coils with radius and coil distance of 350 mm
- Single-layer winding of Litz wire (17 turns per coil)
- 4 mm inter turn pitch, as a compromise between field uniformity and low inter turn stray capacitances
- Support of high density polyethylene, coupling low electrical permittivity ($\varepsilon_r \sim 2.4$)

A close view of the Litz wires and the optimized design of the wire support arrangement with detailed parameters are shown in Figure 4.1b, These solutions allow to minimize the *skin effect* in the supply currents, as well as the influence of stray parameters (especially capacitances).

Frequency (kHz)	1	50	100
Uncertainty (10^{-3})	2.0	4.0	12

Table 4.1: Relative expanded uncertainty (k=2) of the field in the system center

Table 4.1 lists the relative expanded uncertainty of the field in the system center. The magnetic field uncertainty is about 1% at 100 kHz, which suggests a nearly unchanged field distribution with the increase of the frequency at low frequency range.

4.1.2 Measurement frame

A wooden frame including several fixed bars and two movable ones has been designed especially for the measurement around the Helmholtz system (Figure 4.2).

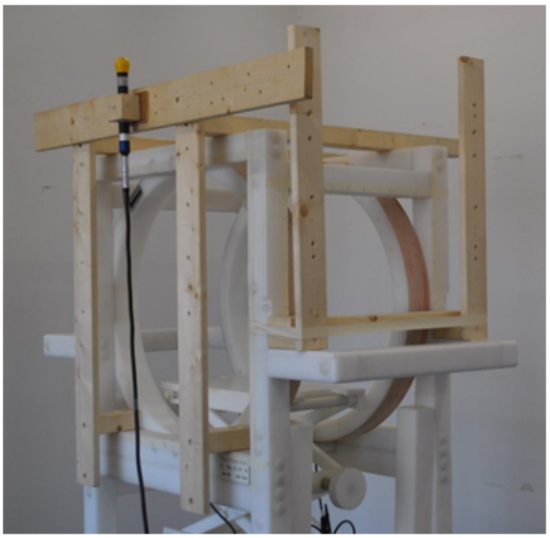

Figure 4.2: The measurement support frame

Three types of supply condition (Supply α, β and γ corresponding to three types of magnetic field distributions) have been applied to the verification process as introduced in the last chapter, by separately supplying the two windings of the system.

In general the field distributions are cylindrically symmetric around z axis for all the supply conditions. As a matter of fact, the fields are symmetric about $z = 0$ plane under Supply α and β. Therefore, a set of measurements performed in the regions A and B indicated in Figure 4.3 contain enough information for a full reconstruction around the Helmholtz coils system, with the assistance of symmetries through x, y, z axises, $x = y$ or $z = y$. It also works on the surfaces in front of the two coils (which include Region A) for Supply γ, while for the other four surfaces, there could be a phase shift of $\pm 90\,^{\circ}$ (various from the components) to the field vectors on region B.

The parallelepiped built by the framework has a dimension of 1040 mm $\times$ 1040 mm $\times$ 800 mm. There is a total of 45 locations where the field are measured indicated as the cross points on the grids in Figure 4.3 (the red ones locate in the common edge). In Region A, the steps of the grid are both 115 mm along x and y axises, while in

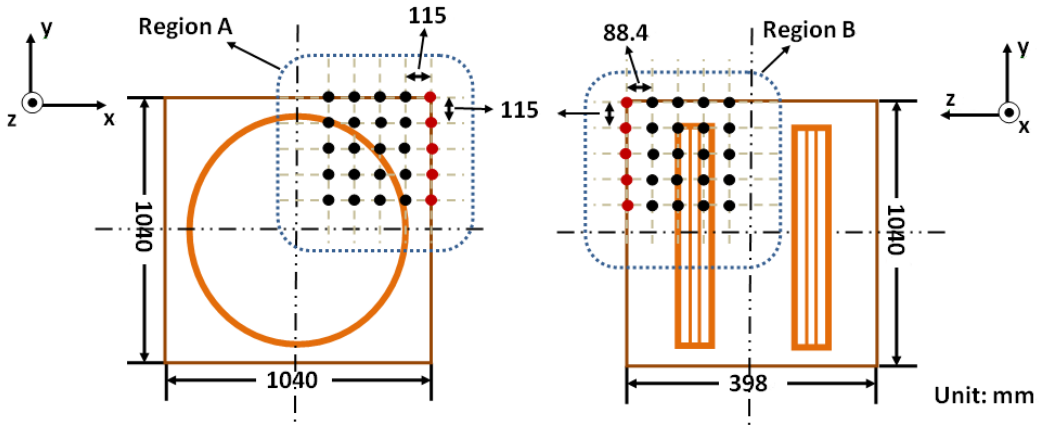

Figure 4.3: Measurement grid

Region B the step along z is 88.4 mm. Through the symmetry, finally 488 points can be received and used as input for the numerical reconstruction procedure.

4.2 Experiment configuration

This section will introduce the detailed experiment process including the method to record the time behaviors of the field vectors which is necessary for BEM reconstruction. All the experiments related to the field measurements and accuracy investigation are carried out in the laboratory of electromagnetic department at I.N.RI.M., where electromagnetic disturbance has been minimized.

4.2.1 Measurement set up

The equipments involved in the supply and measurement circuits are listed below.

- Fluke 5500A Multi-Product Calibrator;
- NF Corporation HSA 4052 (High Speed Bipolar Amplifier DC to 500 kHz) with Maximum current 2 A (rms);
- Guideline 7320 AC Current Shunt (0.1 Ω 10 W);

- Narda ELT-400 Exposure Level Tester, three-axis magnetic field meter (bandwidth 10 Hz to 400 kHz) equipped with a 3 cm concentric coil probe and analog outputs;
- NI cDAQ-9188 and NI 9223 (4-Channel, 1 MS/s, 16-Bit Simultaneous Analog Input Module with input range ±10 V).

Sinusoid signals are generated from the calibrator (5500A), pass through the amplifier (4052) and then supply separately the two windings (which can be connected in series or parallel) of the Helmholtz system. The shunt 7320 is series connected to the coils. The main circuital parameters and the corresponding generated magnetic flux density are listed in Table 4.2.

Type	**Value**	**Unite**	**Explanation**
Frequency	100	Hz	
Gain	20		Amplifier
Current	1.5	A	
Shunt	0.1	Ω	
Inductance	0.5	Ω	Helmholtz coils
B_0	65	μT	Center of the coils

Table 4.2: Input parameters

The measurement circuit consists of ELT-400 and acquisition system(9188 and 9223) from NI. The first three channels of 9223 board acquire the voltage signals corresponding to the three components of the field vector detected by the probe with a cut-off frequency of 10 Hz, and the last one records the voltage drop across the reference shunt (through which the supply current flows), and is used as a trigger for the other three channels in order to record the phase difference from each field component. The input voltage level for all the channels is under ±1.5 V.

The 3th order Butterworth filter inside the field meter ELT-400 offers three options of low cut-off frequency, 1 Hz, 10 Hz or 30 Hz. Figure 4.4 shows the meter frequency responses under 10 Hz and 30 Hz.

Apparently if the meter works under 30 Hz, the output signals can be well filtered. However, since one signal (the trigger) doesn't pass through the filter, a phase shift for more than 30° will appear among the signals. This shift might bring difficulties

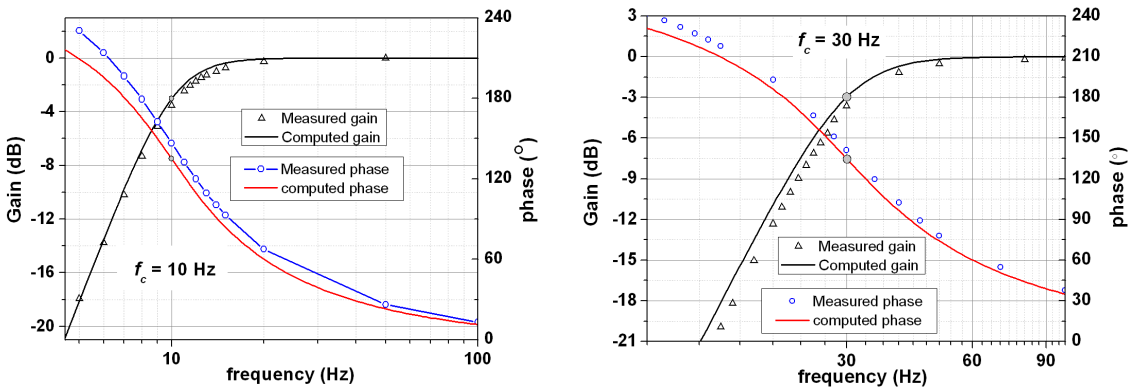

Figure 4.4: Frequency response for $f_c = 10$ Hz and $f_c = 30$ Hz

during the calculation of the phases for the field components which is essential for field reconstruction procedure. On the contrary, with 1 Hz, the filter doesn't work well with relatively weak signals, even though the synchronization is the best of the three. The compromise is 10 Hz, which has been adopted during the field measurement, for smaller phase shift and acceptable noise level. The phase shift during the magnetic field measurement have been investigated in the following subsection.

4.2.2 Python programming

Python is a powerful interpreted programming language, with full modularity and high level dynamic data types. Moreover, the extension modules can be written in Language C which is also supported by the NI-DAQmx driver shipped with the acquisition chassis (cDAQ-9188).

The first task for the programming is data acquisition which must go with the C modules offered by NI. Four channels are sampled in parallel lasting 0.4 s for each measurement point on the grid. 5000 samples for each channel are stored in four arrays once. After transformation of the relative coordinate system of the field meter and the application of sinusoidal fit function, a group of rebuilt sinusoid waves can be received for each point. (The transformation method has been specified in the last chapter.)

Three groups of sequences obtained from different locations in Region A when the coils are series connected (Supply α) and the other three in Region B when the coils are parallel connected (Supply β) have been plotted in Figure 4.5. For each group, the voltage signal (marked as 'V') coming from the shunt has been rescaled to adjust

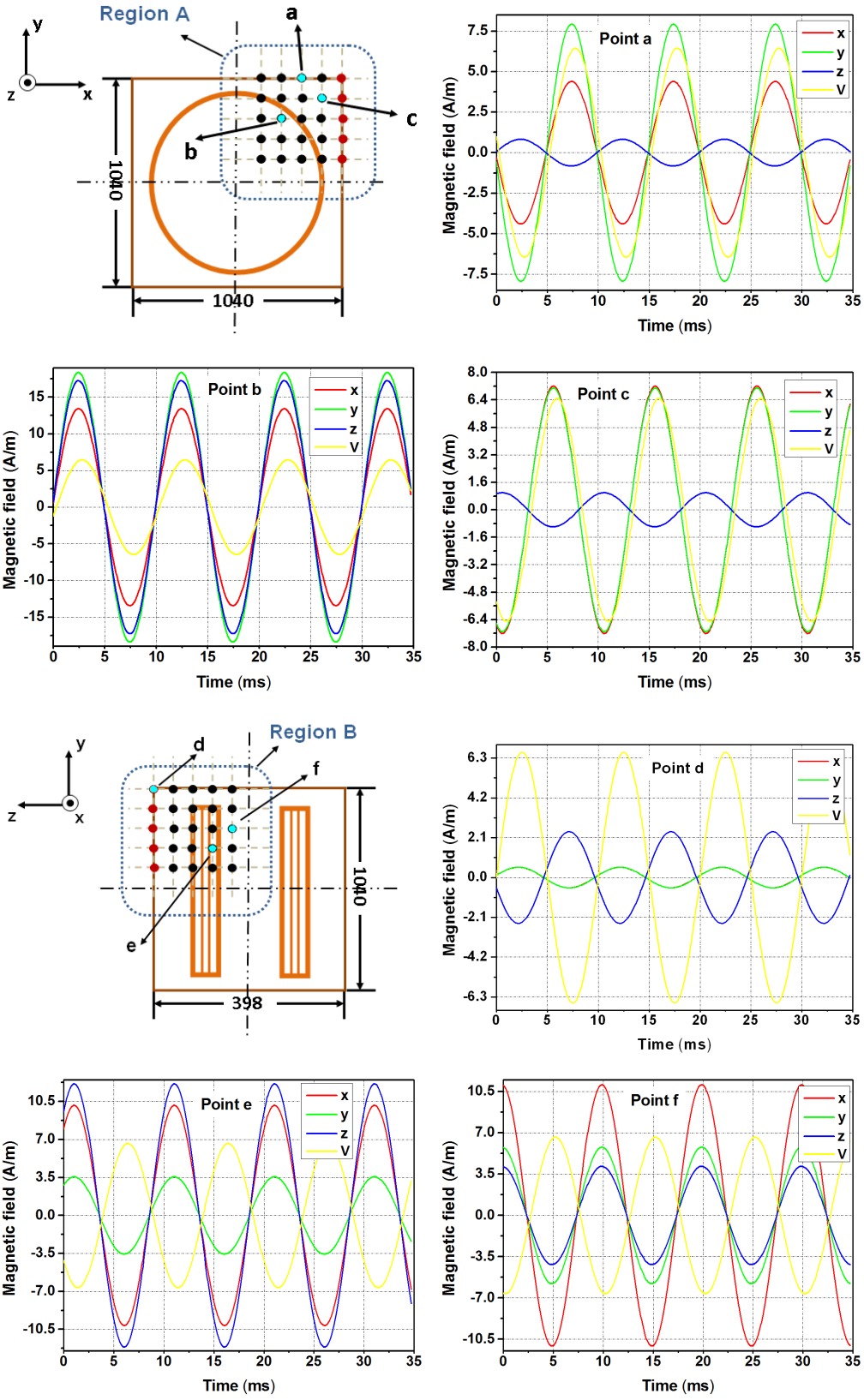

Figure 4.5: The output sequences at different locations in Region A and B

the other three, since only the phase differences from the other three components is required for the reconstruction. The output waveform of this signal is not exactly in phase with the others, due to the delay between the supply and the measurement circuit caused by the field meter.

The phase shift (less than 14° at 100 Hz) caused by this delay can be easily avoided in Supply α and β, with the assumption that the phase differences from the field signals are either 0° or 180°. That is, define a threshold (e.g. 30°), if the actual difference is larger than it, the field sequence will be assigned to 180° phase, otherwise there is no phase shift(0° phase).

Index	**Component**	**Position(m)**	**Magnitude (A/m)**	**Δ**(°)	**Phase** (°)
a	x	0.289	4.40	13.1	0
	y	0.520	7.92	13.0	0
	z	0.398	0.78	-166.3	180
b	x	0.173	13.4	13.1	0
	y	0.289	18.4	13.1	0
	z	0.398	17.3	13.1	0
c	x	0.404	7.16	13.1	0
	y	0.404	7.06	13.1	0
	z	0.398	0.99	-166.3	180
d	x	0.520	0.68	13.3	0
	y	0.520	0.67	12.7	0
	z	0.398	3.04	-167.0	180
e	x	0.520	10.2	-166.9	180
	y	0.173	3.56	-166.9	180
	z	0.133	12.1	-166.9	180
f	x	0.520	11.1	-166.9	180
	y	0.289	5.78	-166.9	180
	z	0.044	4.17	-167.0	180

Table 4.3: The field vectors after phase calculation

Table 4.3 reports the exact locations, the magnitude, phase difference (Δ) and phases in these locations following this phase calculation method. Point a and c on Region A with Supply α have the same phases but different magnitudes for all the components. In these two locations the field values fall mainly on the x and y components,

for the magnetic flux lines have just come out of the coil along these two directions. The z component is relatively weak and has 180° rotation which means the field is just about to turn on this direction. At Point b, all the components are in the same phase with more or less same magnitude. Because the point locates inside but closely to the coil center and the flux lines are going out. These characters coincide with the actual field distributions under Supply α. In fact, under Supply β and γ, the same phase distributions can be found in the same region.

Point d, e and f belong to Region B with Supply β. As mentioned before, at this area, the field distribution is more complicated than under Supply α. At e and f, all of the field components turn to reverse directions. The only difference is at Point e, the field strength of x and z components keeps the same level (10 A/m and 12 A/m), while at Point f, the z field component reduced sharply (4.2 A/m), which means a high gradient exists near these two locations along the main axis. At y component the field strength is always the weakest among the three, since the locations of these points are closer to z-axis. At Point d, the phases of the three field components are identical to Point c, but the field strength level are exactly opposite. It demonstrates the trend that the magnetic flux lines are turning from xy-plane to the main axis z.

Taken reference from Δ in Table 4.3, the phase shift caused by the Butterworth filter inside the probe is $13.2° \pm 0.5°$. This conclusion is useful in the situation that the magnetic sources are not in phase (e.g. with the presence of more than one sources), a correction factor (about -13.2°) must be added to the phase for each field component, in order to calculate the actual phase differences to the trigger signal.

The output of Python program is a list of 45 measurement points, including the locations and complex numbers for all three components of the detected fields.

The interpolation/extrapolation method is then applied on the virtual parallelepiped surface by surface right after the symmetry process which increased the input number of points to 488. This part is accomplished by Matlab for its convenience in dealing with matrix.

In the last chapter, there is the detailed method to obtain 488 points on the virtual surface taking advantage of the symmetric feature of the field distributions around Helmholtz coils system.

4.3 Results and discussions

4.3.1 Magnetic field reconstruction

The dimension of the virtual parallelepiped has been enlarged to adjust the wooden support frame (from 720 mm× 720 mm× 540 mm in the last chapter to 1040 mm× 1040 mm × 800 mm). A larger surface helps to avoid high field gradients which effect the detecting accuracy of the field meter.

Meshes (elements) with two different sizes (both right triangles) have been applied to the virtual surface, corresponding to the amount of 1040 and 160 meshes in total. Apart from the BEM computation starting from the meshes directly, there is also the one through interpolation/extrapolation, with 152 points on a regular grid to reach to 1040 points located at the barycenter of the triangular elements. The field vector on each element is provided by Biot-Savart Law, as well as the fields on each node of the regular grid.

The accuracy investigation of the different reconstruction input mentioned above has been carried out along two lines lying outside of Surface A and B respectively, indicated as Line A and B in Figure 4.6. Both lines have a distance of about 0.7 m from the axises.

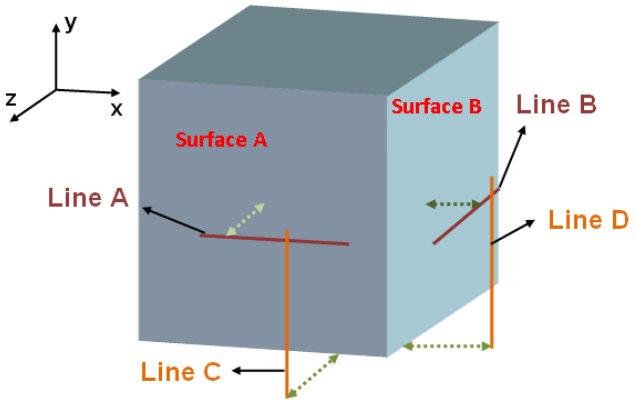

Figure 4.6: Scheme of the positions of the investigation lines

The local error along Line A and B is evaluated as Eq. 3.1, with the reference coming from computation through Biot-Savart Law directly. Table 4.4 reports the average error of the reconstruction results under Supply α, β and γ.

Supply	Line	1040 Points	160 Points	152 to 1040
α	A	0.24	1.25	0.59
	B	0.28	3.27	0.70
β	A	0.35	2.41	1.41
	B	0.79	5.51	1.96
γ	A	0.19	1.16	0.41
	B	0.36	1.57	0.73

Table 4.4: Average error under different supply conditions (in percent)

Apparently, the reconstruction result coming from 1040 points (elements) better agrees with Biot-Savart computation. With similar number of input elements, the reconstruction result through the interpolation method has better accuracy, which coincides with the conclusion from last chapter.

In the following, the reconstruction results from measurement refers to the one through interpolation from 488 points (original 45 measurement points) to 1040 points which are located in the barycenter of the elements discretized all over the virtual surface.

The comparison between simulation and measurement has been performed on two surfaces (Surface M and N) which are parallel to Surface A and B respectively, having the same distance as the investigation lines (Line A and B indicated in Figure 4.6) with respect to the axises.

There are two groups of magnetic field(H_{peak}) distributions over Surface M with different supply conditions in Figure 4.7. The one given by applying the Biot-Savart directly on the sources is on the left, the one obtained from BEM reconstruction procedure on the right. Each row refers to one type of supply condition with the order of α, γ and β (normalized to same current value in each coil before the reconstruction) from top to bottom.

The field distributions are similar to each other for different supply conditions generally. The Biot-Savart results (the left column) demonstrate that the field strength trends to decrease along radius, and reduces gradually through three supply conditions. The reconstructed results (the right column) have similar characteristics, although the field values are always slightly lower than the Biot-Savart ones because of the approximation procedure applied by BEM. The field distribution (especially around 1 A/m)

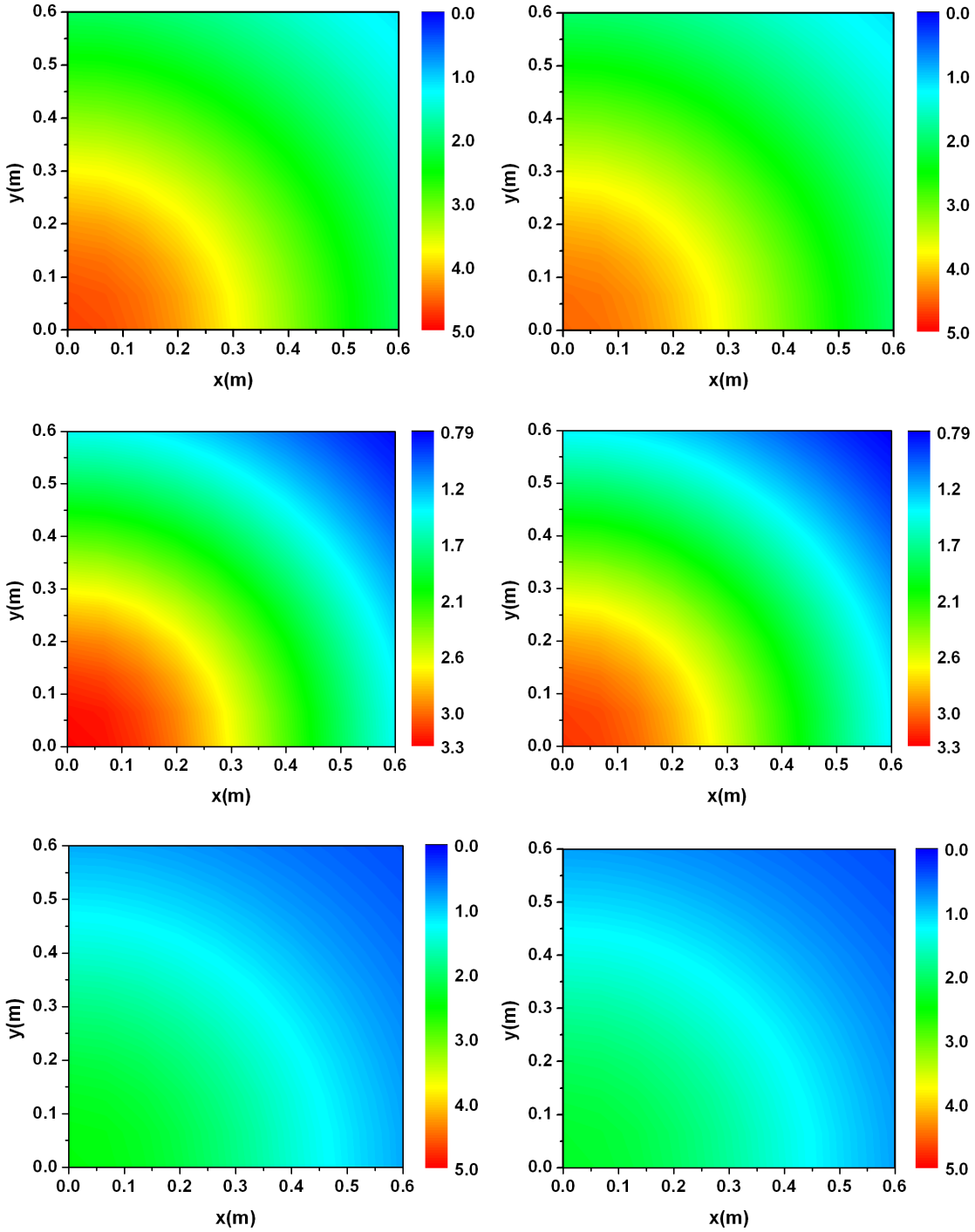

Figure 4.7: Magnetic field amplitude (A/m, *peak*) distributions on Surface M

appears to have a little displacement comparing with simulation, especially with Supply β, where the field level is the lowest among the three supply conditions. This disagreement probably comes mainly from the measurement sensor, whose accuracy is more affected in low field range by non-negligible wide band noise. It is not difficult to conclude that the best agreement comes from Supply α, which has the highest field level.

Figure 4.8 presents the field distribution (H_{peak}) on Surface N, under the same order of supply (α, γ and β), with Biot-Savart result on the left and BEM reconstruction on the right.

Overall, the field level is more than half lower as that on Surface M but mostly above 1 A/m, and the field distributions are various for each supply condition. The highest field strength still can be found under Supply α since the identical currents flowing in the two coils strengthen the resultant field for each other, while the relatively weak field exists again in Supply β due to the exactly opposite phases of the currents. Although the field distributions are in good agreements, the reconstruction results are always slightly lower, and the the layout of field gradients are less distinguishable, such as near the y-axis about 0.3 m from the origin under Supply α and γ, comparing with computation directly from Biot-Savart Law.

The discrepancy is evaluated according to Eq. 3.1, only exchange the simulation data to real measured one.

Figure 4.9 shows the local discrepancy distributions both on Surface M and N (left and right column respectively), supplied by α, γ and β for each row of three. Here the reference is the computation results from Biot-Savart Law. In general, the discrepancy is less than 7% for all the supply conditions, which demonstrates a good reconstruction quality.

For Supply α, on the Surface M, where the field values are the highest comparing with the other two supply condition, the discrepancy has an average distribution around 3.8%. While on the other surface N, the largest discrepancy appears in the area close to the winding (z=0.35) where higher gradient are present (upper half of the surface).

The discrepancy level increases under Supply γ over Surface M, and the distribution is no longer uniform. More regions with higher discrepancy($\eta > 4.3\%$) are present along $x = 0$ and even the region with relatively lower discrepancy($\eta < 3.0\%$) near $x = 0.6$ enlarges. It means with higher field level (e.g. under Supply α), the proposed procedure

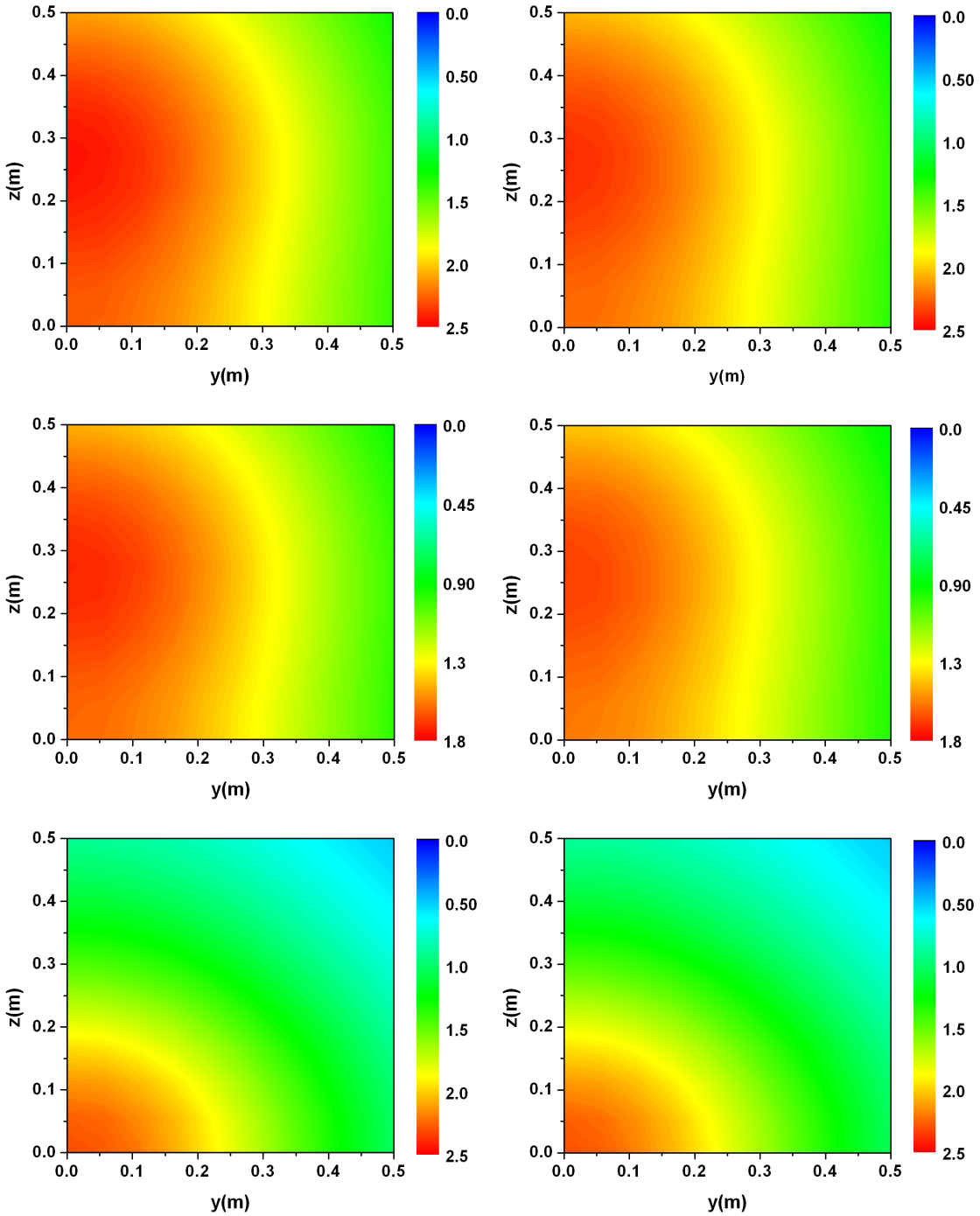

Figure 4.8: Magnetic field amplitude (A/m, *peak*) distribution on Surface N

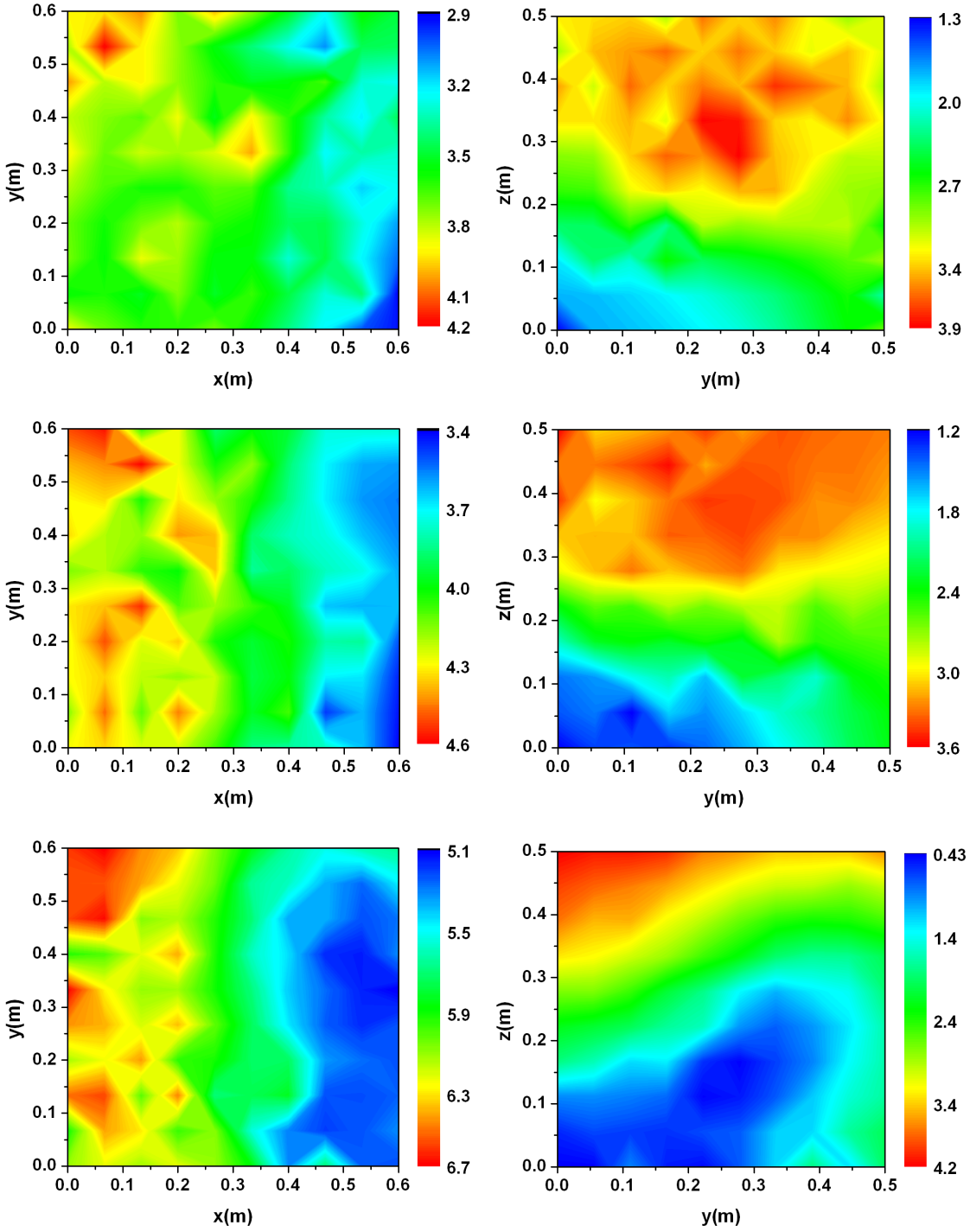

Figure 4.9: Discrepancy(in percent) distribution on Surface M and N

has better performance. Unlike on Surface M, the discrepancy remains in the same level as Supply α. However, the larger discrepancy region ($\eta > 2.9\%$) almost takes up all the upper part of the surface, since even with similar field gradient, it brings difficulties in reconstruction the complexity (rotation), as well as lower level of the field.

As for supply condition β, the discrepancy drops on both surfaces. The maximum happens over Surface M, with similar distribution as previous two but larger values, which is reasonable due to the field level is the lowest among the three.

On Surface N, the largest discrepancy presents under Supply β, as well as the smallest, which suggests an relatively unstable reconstruction. And the distribution differs from the other two. That's because the field level is lowest of all , and the field distribution is completely different where highest field gradient presents.

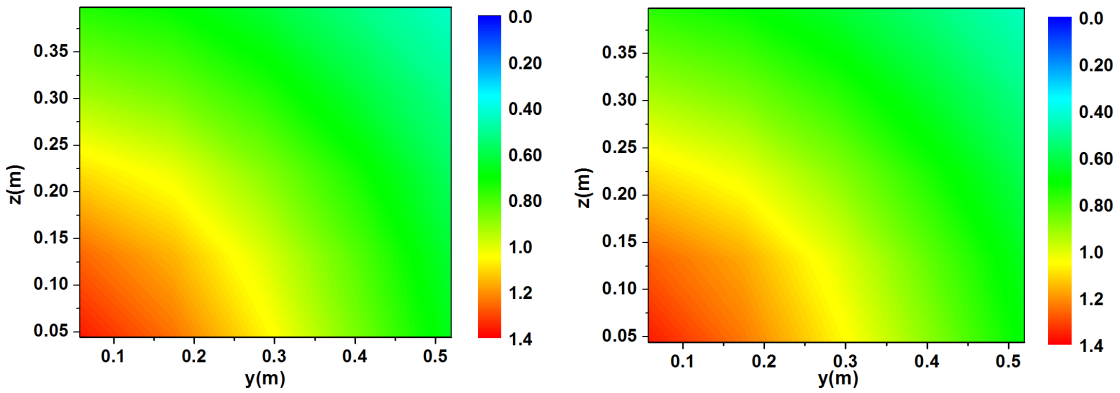

Figure 4.10: Measured and reconstructed field distributions (A/m, *peak*) on Surface N'

Under consideration the critical situation appeared on Surface N under Supply β, the reconstruction quality has also been examined directly through measurement on a surface paralleled to Surface N, Surface N', making use of an extension wooden bar attached on the movable one, so that there is a distance of 0.31 m from the measurement frame. Figure 4.10 shows the comparison of the magnetic field distribution on this surface through measurement (left) and reconstruction (right).

The field distributions from both are the same as in Figure 4.8, only with lower field level, since Surface N' is further away from the source than N.

The discrepancy distributions in Figure 4.11 are evaluated following Eq.3.1, both taking reference from measurement directly on this surface. In general, the maximum

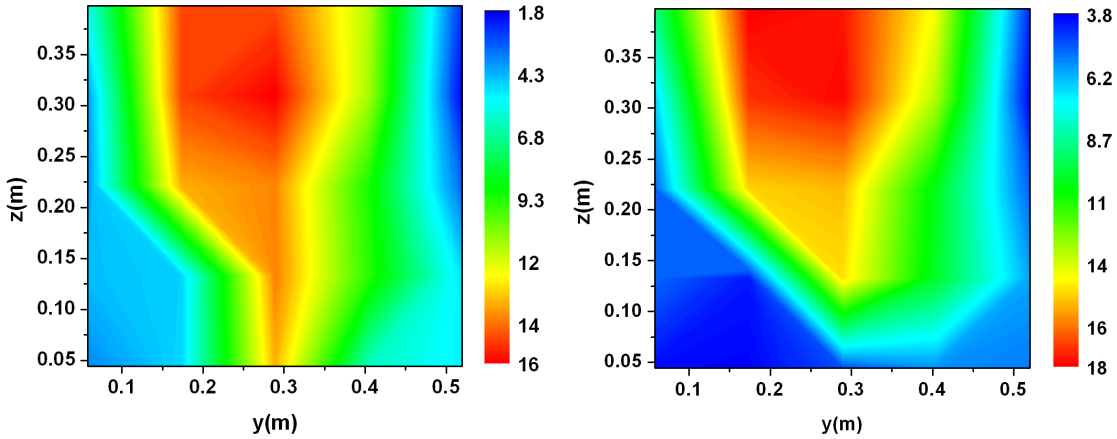

Figure 4.11: Discrepancy distribution (in percent) of computation through Biot-Savart (left) and reconstruction (right) on Surface N'

discrepancy ($\eta = 15.8\%$ for reconstruction and $\eta = 17.9\%$ for Biot-Savart) always happens where the winding of the Helmholtz system locates. The result from reconstruction procedure has a similar distribution (with few percentage more) to the one computed directly from Biot-Savart, which means the disagreement from the reconstructed field to simulation is mainly caused by the measurement error.

In theory, the proposed field reconstruction procedure can be applied to any kind of electromagnetic sources and have passive elements included. Two stacks of ferromagnetic sheets have been included on Surface A and C (the symmetric surface of A about $z = 0$ plan) respectively, in order to examine the reconstruction ability around non linear sources (which include also passive objects with high permeability materials and eddy currents). Each stack consists of six 0.30 mm GO Fe-Si laminations (electrical resistivity $\rho = 48 \times 10^{-8}$ Ωm); the laminations arranged rolling along x and y alternately. 1 kHz current has been applied to serially connected Helmholtz coils, so that more the eddy currents appear in the material. The other input parameters remain the same as in Table 4.2. The phase shifts between the field component and the reference are different from Table 4.3 (within 7° delay), because of the presence of eddy currents. On the other side, it has been verified that the iron saturation doesn't quite give rise to waveform deformation. The symmetry of the field distribution still exits on the same surface and among the surfaces because the sheets are located on two symmetric surfaces.

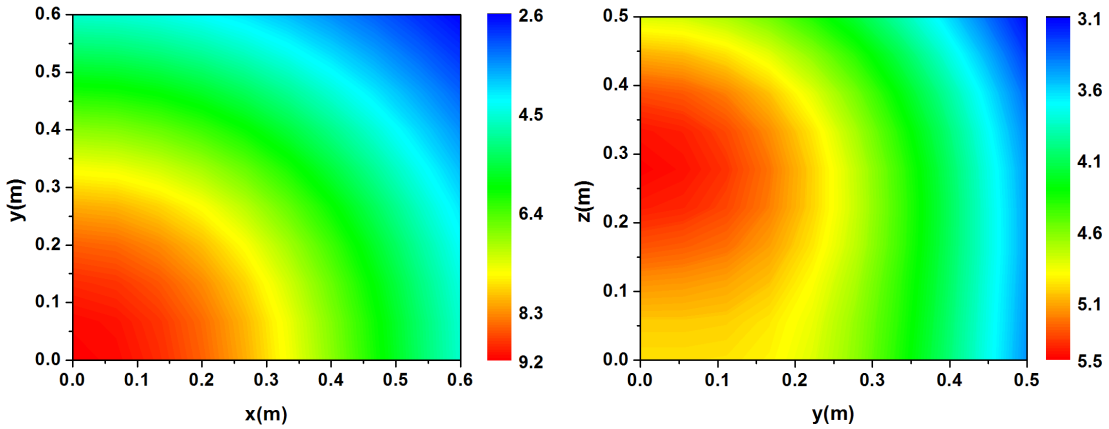

Figure 4.12: Magnetic field distribution (A/m, *peak*) on Surface M and N when non-linear materials present

The amplitude of magnetic field on investigation surfaces M and N are plotted in Figure 4.12. The field values increase significantly for both surfaces, while distribution has not been modified (taking reference from Figure 4.7 and 4.8).

Figure 4.13 illustrates the comparison between measurement and reconstruction magnetic field along Line C ($x = 0.36$, $y = -0.5 \sim 0.0$, $z = 0.58$) and D ($x = 0.67$, $y = -0.5 \sim 0.0$, $z = 0.17$) as depicted in Figure 4.6, where the field gradient should be intensified by the ferromagnetic materials. Better accuracy can be found in Line

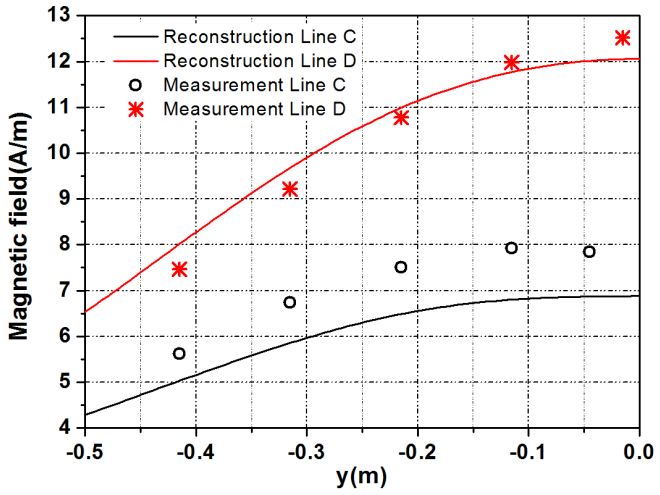

Figure 4.13: Measured and reconstructed magnetic field amplitude along Line C and D

D where the local error η is always less than 5%, while along Line C, it could achieve $\eta = 16\%$[47].

4.3.2 Induced electric field evaluation

The investigation of induced electric field when human body is exposed to low frequency (100 Hz) unknown magnetic sources has been carried out based on the reconstruction results around the Helmholtz coils system. The human model adopted during the evaluation has been specified in Chapter 2.

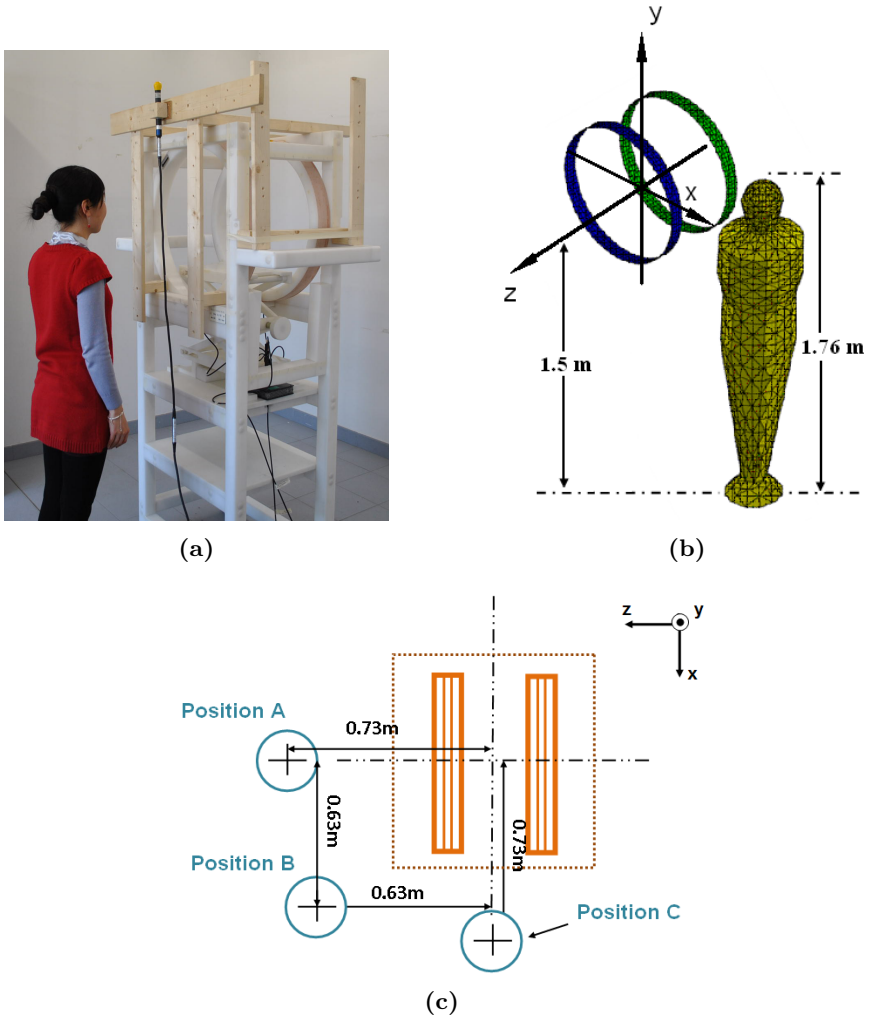

Figure 4.14: Reconstructed and measured field distributions on Surface N'

As the frequency increases, the magnetic field distribution produced by the standard field generation system is nearly unchanged up to some ten kilohertz as shown in Table 4.1. Even with the presence of the human model, the magnetic field generated by the induced currents has been assumed to be negligible, since it's considerably weak if compared with the one generated from the source (Helmholtz system). It has been proved numerically that the assumption remains valid in the same frequency range. As a result, only the amplitude of the induced electric field within the homogeneous body increases linearly with the frequency.

The body has been presented in different position regarding the Helmholtz coils as shown in Figure 4.14. Figure 4.14a shows a real example of the relative position involving the magnetic source (Helmholtz system) and the human body. The human model has a height of 1.76 m from the ground, while the Helmholtz system has 1.5 m vertical distance from z-axis to the ground (Figure 4.14b).

The three positions of the human model has been depicted in Figure 4.14c. For Position A, the model presents right in front of one of coils with 0.73 m distance along $z > 0$. Position B is located in the diagonal direction with respect to the coils. And with Position C, the model faces the $x = 0$ plane, with 0.73 m far from the origin along $x > 0$.

At each position, for each supply condition (Supply α, β and γ), the electric field induced inside human model has been evaluated starting from the surrounding magnetic field distribution received by three different procedures. Firstly, the applied fields are computed directly from the currents flowing in the Helmholtz through Biot-Savart Law, which can also provide the field located on the measuring frame. And then making use the reconstruction method, the magnetic field distribution all over the body can be received (second procedure). As the last procedure, the computed field vectors on the measurement grid are replaced by real measurements .

The accuracy is evaluated through Eq. 4.1,

$$\eta_e = \frac{|\sqrt{\sum_{k=1}^{3}[(E_{k,r}^{S})^2 + (E_{k,i}^{S})^2]} - \sqrt{\sum_{k=1}^{3}[(E_{k,r}^{R})^2 + (E_{k,i}^{S})^2]}|}{\sqrt{\sum_{k=1}^{3}(E_{k,r}^{S})^2 + (E_{k,i}^{S})^2}} \tag{4.1}$$

where superscripts S and R indicate the results received from the first procedure (which assumed to be reference) and the third one, subscript k denotes the three components

(x, y, and z), while the other two refers to real (r) and imaginary (i) part of the field vector.

First of all, both the magnetic field and induced electric field have been evaluated at Position A under Supply α, along the line $x = 0.01, y = -1.4 \sim 0.2, z = 0.74$. The amplitude of the magnetic field and electric field received through various procedures has been plotted in Figure 4.15, together with half of the human profile, whose height coincides with the vertical axis (y-axis).

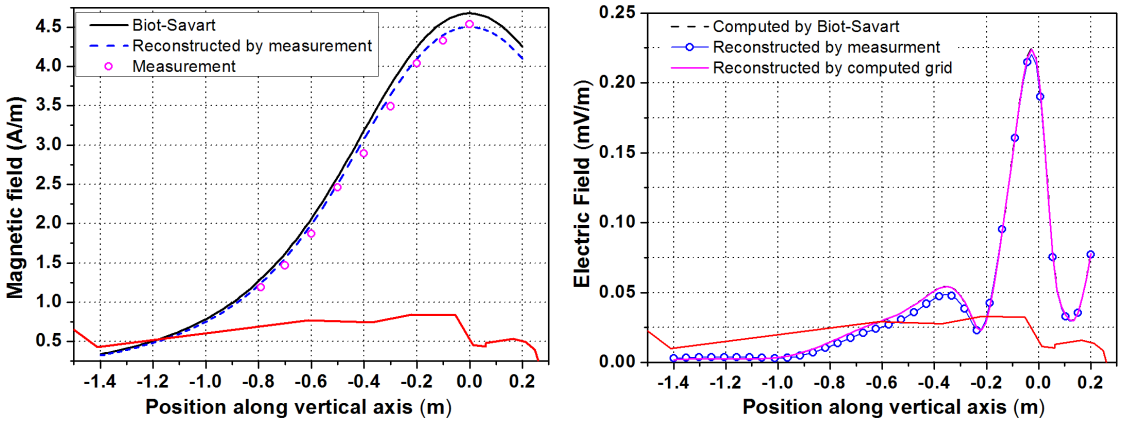

(a) Amplitude of magnetic field (*peak*) **(b)** Amplitude of induce electric field (*peak*)

Figure 4.15: Magnetic field and corresponding induced electric field under Supply α

The reconstructed magnetic field through actual measurement has been compared with the simulative results and some measurement points directly along the investigation line (Figure 4.15a), and again shows good agreement. The induced electric field (Figure 4.15b) along the same line rises gradually from the ankle, decreases suddenly between upper arm and shoulder, and then reaches the maximum at the base of neck and drops significantly right after.

The computation results from the first two procedures (related to Biot-Savart Law) can barely be distinguished from Figure 4.15b, which suggests a good accuracy of the BEM reconstruction. The relative discrepancy η_e associated with the practical measurement has an average of 1.71% while the amplitude is higher than 7×10^{-5} V/m, which is more than satisfactory taken into account the measurement uncertainties.

Figure 4.16 shows the induced electric field along two lines near the central axis of the human model in Position B and C. The field level is half to the one in Position

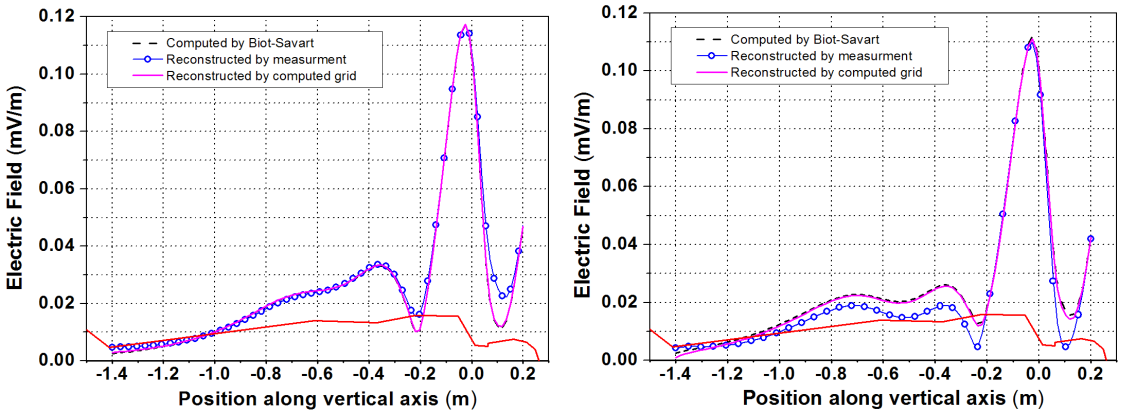

(a) Induced electric field in Position B

(b) Induced electric field in Position C

Figure 4.16: Induced electric field (*peak*) in Position B and C under Supply α

A, while the behavior of the amplitude is almost the same. Superb accuracy still can be found within the results obtained from reconstruction procedure starting from simulative field vectors (the second procedure).

The average relative discrepancies when the field level is above 5×10^{-5} V/m are $\eta_e = 1.37\%$ for Position B and $\eta_e = 3.54\%$ for Position C. The largest discrepancy appears when the amplitude is below 4×10^{-5} V/m, while the maximum could reach 1.17×10^{-4} V/m for Position B and 1.12×10^{-4} V/m for Position C.

More comparisons have been taken out through Supply β and γ. Figure 5.1 plots the amplitude of induced electric field along the same line as that under Supply α in Position C, where the field gradient distributions are various.

The electric field behaves almost the same as previous computational results, only the field level drops again under Supply γ. At relatively high field level ($> 5\times10^{-5}$ V/m for Supply β, $> 4\times10^{-5}$ V/m for Supply γ), the relative discrepancies are respectively 0.45% and 2.68% in average.

The good agreement between Biot-Savart computation and BEM procedure with computed field vectors on the measuring grid (the first and second procedure) means that the approximation and interpolation during the reconstruction process hardly make influence on the accuracy of the electric field evaluation. In the meanwhile, it also suggests that the discrepancy during the reconstruction through real measurement points comes mainly from practical experiments. Anyway, a satisfactory agreement

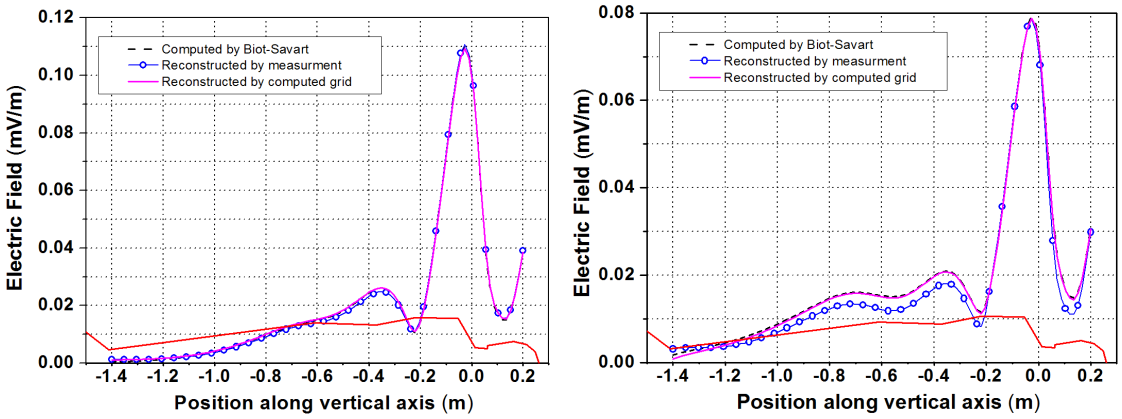

(a) Induced electric field (Supply β)

(b) Induced electric field (Supply γ)

Figure 4.17: Electric field distribution (*peak*) in Position C under Supply β and γ

still can be found in measurement especially with relatively high field level for all the considered situations.

A further investigation on the induced electric field distribution and accuracy over cross-session of the human model is reported in Figure 4.18[48].

The accuracy has been evaluated through relative deviation ξ_e defined as Eq.4.2,

$$\xi_e = \frac{\sqrt{\sum_{k=1}^{3}[(E_k^S)^2 - (E_k^R)^2]}}{|E_{max}|} \tag{4.2}$$

where superscripts S and R and subscript k are the same as Eq.4.1, while E_{max} denotes the absolute maximum electric field amplitude over the region evaluated through the first procedure mentioned before.

The induced electric field has a symmetric distribution over the plane normal to x-axis in Figure 4.18a, since the magnetic field is in symmetry about $z = 0$ plane under Supply β, and so is the human model positioned at C. As for Supply γ, the rotating magnetic field gives rise to a non-symmetric electric field within the cross-session of the body located in Position C. The electric field levels are almost equal in these two investigation areas.

The relative deviation ξ_e distribution of over the same cross-session in Figure 4.18a is also symmetric about the central axis of the human model as shown in Figure 4.18c. For the same position under Supply γ, higher discrepancy appears only at one side of

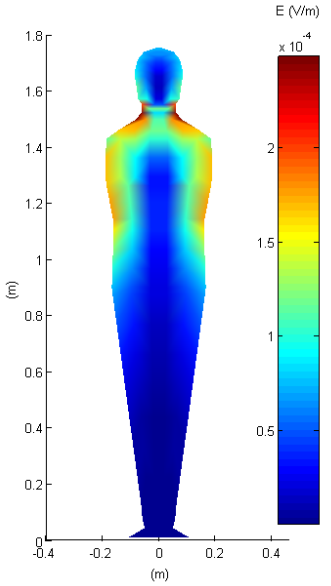

(a) Electric field (per-unit current) distribution over yz-plane computed through Biot-Savart Law in Position C under Supply β

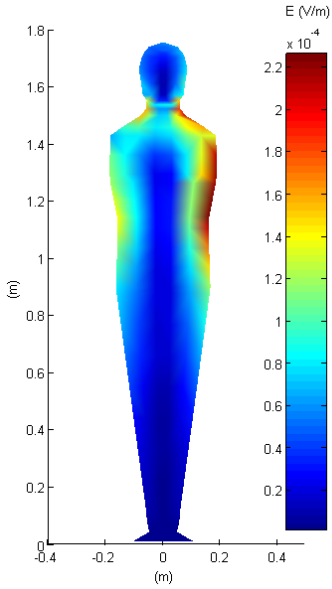

(b) Electric field (per-unit current) distribution over yz-plane computed through Biot-Savart Law in Position C under Supply γ

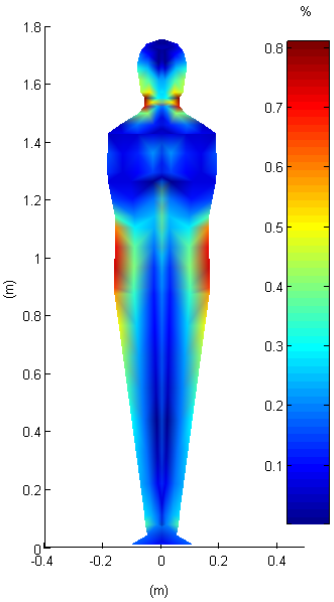

(c) Distribution of relative deviation ξ_e (in percentage) in the same area of (b)

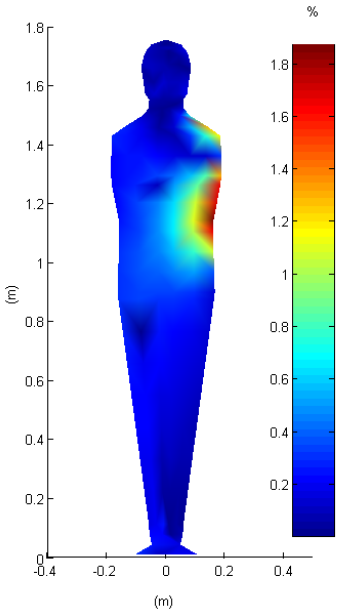

(d) Distribution of relative deviation ξ_e (in percentage) in the same area of (a)

Figure 4.18: Electric field and relative deviation ξ_e distribution over two cross-session of human model

the cross-session near the arm and elbow (Figure 4.18d). However, the value is always lower than 2% for both two supply conditions.

5

Prediction of emissions at High Frequency

5.1 Introduction

In high frequency range, the radiation emissions produced by any kind of devices can be predicted by this hybrid procedure. The accuracy of the prediction has been examined based on some international standards related to radio frequency limits and measurements in the electromagnetic compatibility (EMC), through the comparison with another kind of numerical method. Taken into consideration the difficulties that might be met during the practical experiments, the accuracy investigations have been carried out also under the condition that the contribution of some points (elements) located on certain surfaces are removed.

Unfortunately, the electric field probe suitable for the 'vectorial' measurement at this frequency range is not ready. Nowadays, measuring the phase of the fields with a satisfactory accuracy is still a challenging subject for many EMC researchers.

5.2 Computational procedure and validation

5.2.1 Radiation sources

Four elementary antennas are assumed as electromagnetic sources which consist of two dipoles and two loops (with positive directions for all). Figure 5.1a indicates the positions of the antennas and also the virtual box (parallelepiped), enclosing all of them,

which has the size approximating a rack (1 m × 1 m × 2 m). The virtual box is assumed

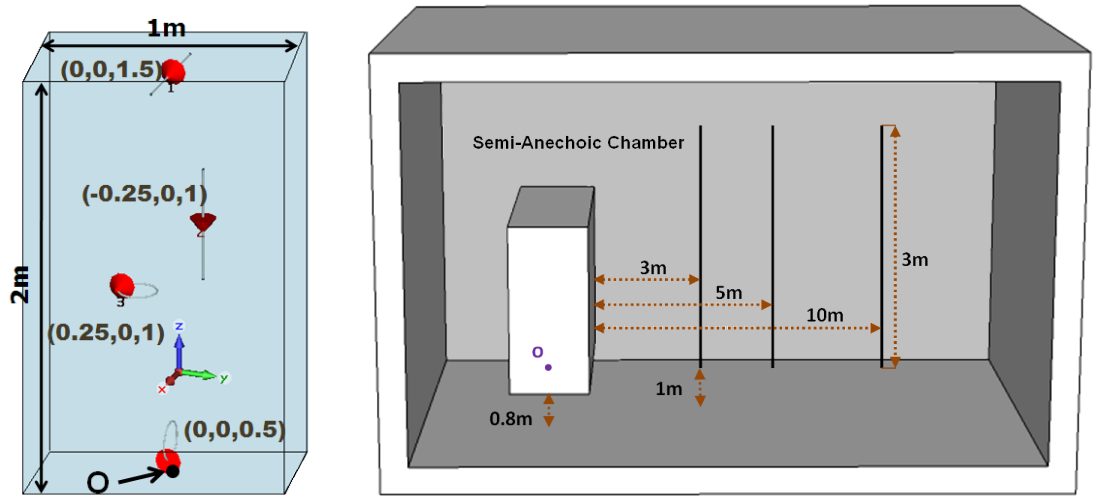

(a) The locations of antennas and virtual box

(b) Scheme of the virtual box and test lines (not in scale)

Figure 5.1: Simulation model at Radio frequency

to be placed at 0.8 m above the ground inside a Semi-Anechoic Chamber (SAC), as shown in Figure 5.1b, where the floor is a metallic ground plane. This is the typical measuring set up used to evaluate the radio frequency emission produced by sources placed on a rotating table at the height of 0.8 m above the ground at distances fixed by international EMC standards. Suitable broad-band receiving antennas connected to a selective receiver or a spectrum analyzer are employed to measure the electromagnetic field strength radiated by the sources. The receiving antenna is scanned along a vertical line from 1 to 4 m to find out the maximum emission.

The supply conditions and corresponding features of the elementary antennas (two 0.1 m diameter magnetic dipoles and two 0.3 m long electric dipoles) have been reported in Table 5.1. The antennas are supplied under three frequencies, 30 MHz, 100 MHz and 300 MHz, with different current peak and phase for each frequency and each antenna. In this frequency range, the field propagation does not always follow the '$1/d$' law of propagation(far-field condition), where d is the distance from the source.

Antenna	30 MHz		100 MHz		300 MHz	
	Peak(mA)	*Phase* (°)	*Peak*(mA)	*Phase* (°)	*Peak*(mA)	*Phase* (°)
1	222	45.7	95.4	150	0.292	-146
2	233	49.4	105	152	0.196	-146
3	4.74	173	16.3	-53.4	1.38	10.3
4	4.74	-7	16.3	126.6	1.38	-169.7

Table 5.1: Supply conditions of the antennas

5.2.2 Numerical modeling

A commercial software CST Microwave Studio (MWS) [49] has been used to build up the numerical model of the electromagnetic sources and to provide the reference during the accuracy evaluation.

CST MWS is a numerical tool for 3D electromagnetic simulation in High frequency, based on Finite Integration Technique (FIT). Open boundary conditions have been applied during the modeling to simulate the free space. A perfect conductive layer which has a large dimension (16 m×30 m) with respect to the virtual box is assumed as the ground.

As for BEM procedure, the image method has been applied to avoid the discretization of the finite ground plane, which would reduce accuracy of the reconstruction and increase the computational burden by requiring an electromagnetic field problem solution instead of a simple reconstruction [50]. The image box has the field components imposed over the surface according to the boundary conditions (Tangential components of **E**-field x and y and Normal component of **H**-field z have opposite direction with respect to the original box).

According to typical EMC assessment tests and standard [51], the accuracy investigations are performed along 3 m long vertical lines as shown in Figure 5.1b, extending from 1 m to 4 m above the ground, having distances of 3 m, 5 m and 10 m respectively from the box (x=0). For each frequency and each investigation line, the reference field values are computed through CST by activating the four antennas one by one, and then making a linear summation of the fields generated from each of them. In the meanwhile, the input field vectors for the BEM procedure are also provided by CST through the same method.

5.3 Results and discussions

As the first step, 500 points (located on the barycenter of the discretized elements) have been applied to reconstruct the field distribution around the antennas. Figure 5.2 shows the comparisons between the electric field simulated by CST and the one reconstructed through BEM procedure along each investigation line.

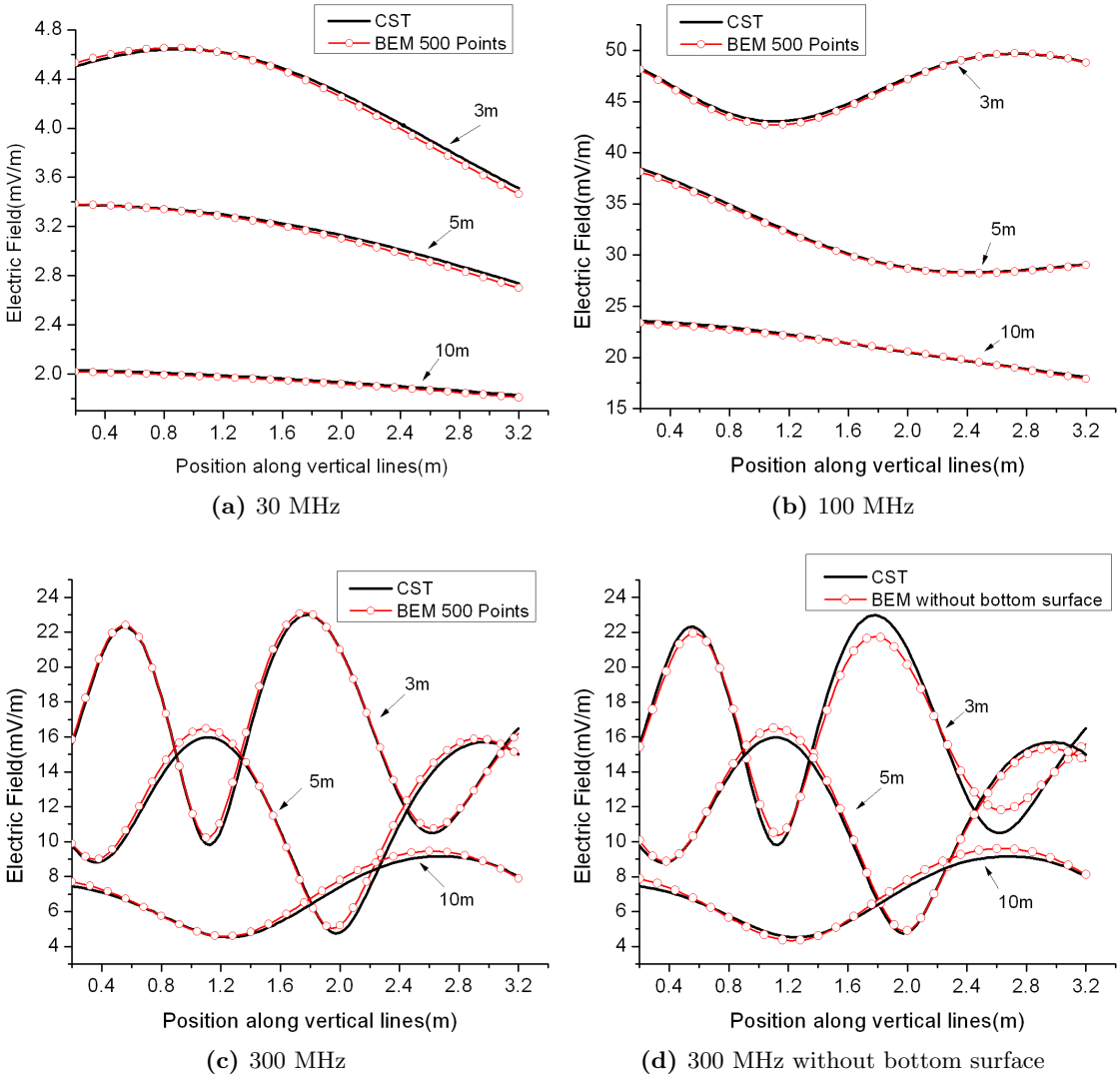

(a) 30 MHz

(b) 100 MHz

(c) 300 MHz

(d) 300 MHz without bottom surface

Figure 5.2: Amplitude of the electric field (*peak*) along the investigation lines

In Figure 5.2a and 5.2b, the antennas have been supplied at 30 MHz and 100 MHz, respectively. Through the field level along each line in both of the two diagrams, it

demonstrates that the '$1/d$' propagation is not valid at a relatively low frequency range, which means the limits are no longer reliable.

Figure 5.2c shows the electric field distribution along the three investigation lines at 300 MHz both from CST and BEM reconstruction as in Figure 5.2a and 5.2b. The propagation law mentioned before is valid under this situation.

Generally, the results from the two different numerical solutions are found to be in good agreement for all the frequencies.

The relative error at 30 MHz increases gradually from the beginning (1 m above the ground) and reach to the maximum at the end (4 m above the ground) for all three investigation lines, with the values of 1.36%, 1.37% and 0.96%, respectively. At 100 MHz, the error distribution is different for each line. The maximum is 1.00% at 10 m investigation line, located near the ground (1.4 m above the ground).

At 300 MHz, apparently, the largest discrepancy appears at 2.1 m (about 3 m above the ground) along 5 m investigation line, where the field value is relatively low. The corresponding relative error is about 11%. However, the accuracy of the proposed method is not influenced by this discrepancy since the aim of the measurement of the EMC test is to search for the maximum field value (in this case 16 mV/m along 5 m line as shown in Figure. 5.2c), where the error is about 3%.

	Remove **back** surface		
	3 m	5 m	10 m
30 MHz	16.4	17.2	17.8
100 MHz	7.24	7.95	6.49
300 MHz	11.8	17.5	10.8
	Remove **bottom** surface		
	3 m	5 m	10 m
30 MHz	5.06	5.13	4.69
100 MHz	10.7	10.2	5.84
300 MHz	12.7	3.96	5.80

Table 5.2: Maximum local error (in percentage) after removing certain surfaces

Taken into consideration the measurement burden and the difficulties to position the probe on the bottom surface during the practical experiments, the field distribution has

been also estimated when the contribution of the points at the bottom surface ($z = 0$) or at the back ($y = -0.5$) are removed.

Figure 5.2d plots the fields along the three investigation lines at 300 MHz without the contribution of the bottom surface ($z = 0$) points (elements). The maximum error is 12.7%, which appears at 2.6 m along the 3 m line (3.4 m above the ground).

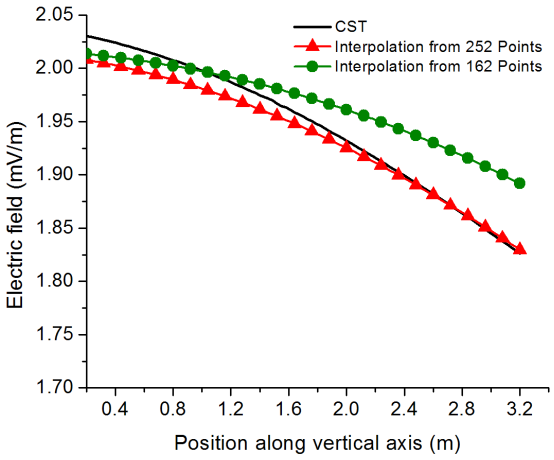

(a) 10 m line at 30MHz

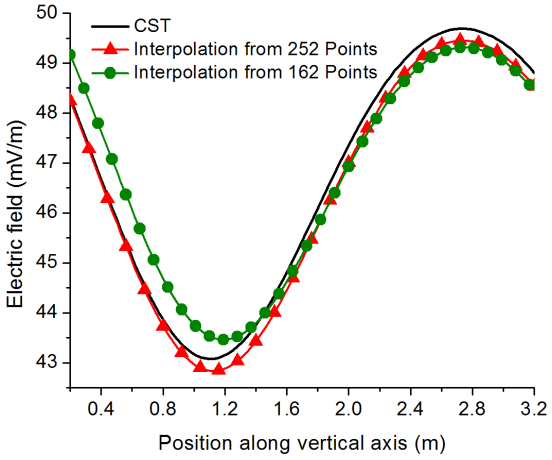

(b) 3 m line at 100MHz

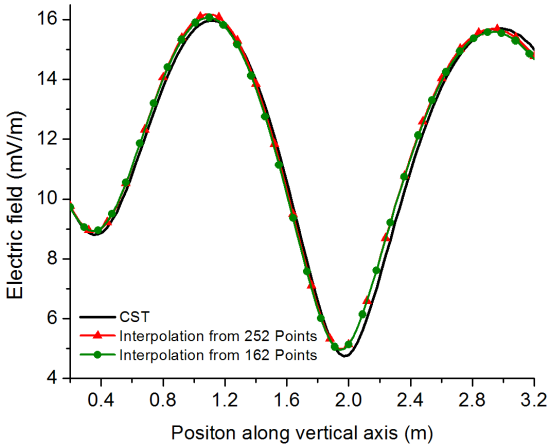

(c) 5 m line at 300MHz

Figure 5.3: Amplitude of the electric field (*peak*) along the investigation lines after applying interpolation

The maximum relative local error along each investigation line after removing the two surfaces has been reported in Table 5.2. When the back surface ($y = -0.5$) has been removed, the predicted field values from BEM reconstruction are no longer reliable

especially at 30 MHz. On the contrary, better accuracy has been obtained without the bottom surface ($z = 0$). Anyhow, in some cases the maximum error exceeds 10%, with the maximum 12.7% among the three supply conditions as shown in Figure 5.2d.

The interpolation/extrapolation method has been applied to this BEM reconstruction procedure in high frequency range as well, in order to simplify the measuring procedure.

The electric field distributions along the three investigation lines after applying the interpolation are reported in Figure 5.3. The comparison is among the simulation of CST, and the results obtained starting from different number of points (252 and 162 respectively) applied in regular arrangement, and then interpolating to 500 points located on the barycenter of the discretized elements to perform the reconstruction.

Table 5.3 reports the maximum error along each investigation line when applying 252 points, 212 points and 162 points respectively for interpolation.

	252 Elements		
	3 m	5 m	10 m
30 MHz	4.06	2.27	1.08
100 MHz	0.81	0.94	1.24
300 MHz	4.89	9.76	3.81
	212 Elements		
	3 m	5 m	10 m
30 MHz	12.6	8.08	2.45
100 MHz	1.19	1.11	1.10
300 MHz	4.79	9.51	3.69
	162 Elements		
	3 m	5 m	10 m
30 MHz	16.2	10.7	3.60
100 MHz	2.12	1.66	1.5
300 MHz	5.19	9.80	4.01

Table 5.3: Maximum local error (in percentage) after applying interpolation

With about half number of measurement points located on a regular grid with respect to 500 points which must be measured at the barycenter of the triangular elements over the discretized surface, the accuracy is satisfactory. When the number of the measuring points has been further reduced, larger discrepancies appear at 30 MHz,

especially when the number reaches 160. It should be noticed that the maximum error always locates where the lowest field value can be found, so the measurement accuracy will not be reduced as discussed before. For example, $z = 3.2$ (4 m above the ground) at 30 MHz 3 m investigation line and $z = 2.1$ (2.9 m above the ground) at 300 MHz 5 m investigation line (Figure 5.3c). Anyway, at 100 MHz, all the cases have excellent accuracy.

6

Uncertainty estimate

6.1 Introduction

The evaluation of the uncertainty in hybrid experimental-numerical procedures is a critical issue, because of the uncertainties associated with the numerical method and the propagation of the measurement uncertainty when processed by a complex computational technique [52]. On the basis of these considerations, values of the order of several percent can be considered quite a satisfactory target for the output quantities of the hybrid procedure[53].

As mentioned before, the main reason to choose Helmholtz coil system as magnetic source is that, due to the strict mechanical tolerance of the realization, its geometry is perfectly known, so that it is able to provide anywhere near the coils the magnetic fields which can be predicted with considerably high accuracy. As a result, the computed field values received from Biot-Savart Law have been taken as a reference for all the comparison and accuracy evaluation procedures in low frequency magnetic field reconstruction procedure.

To evaluate the output quantity (electric field inside human model), the measured magnetic fields has to be processed through three numerical steps (interpolation, BEM reconstruction and BEM electric field solution). The complexity of this whole procedure suggests that the commonly used law of uncertainty propagation approach provided by GUM [54] is no longer suitable.

This chapter will discuss about the uncertainties caused by discretization of the numerical procedure and the magnetic field measurement as well. The propagation

distributions through the computational process due to measurement operations are estimated based on Monte Carlo Method, exploiting again the magnetic fields around the Helmholtz model computed through Biot-Savart Law. Making use of the linearity of the entire numerical procedure, the computation time can been significantly reduced. The proposed procedure can be applied to estimate the measurement uncertainty for both the reconstructed magnetic field and induced electric field, although the experimental validation can be only performed for field reconstruction.

6.2 Monte Carlo Method (MCM)

Monte Carlo Method as considered here is regarded as a means to propagate the input uncertainties of the considered problem through the numerical model and evaluate the best estimate for the output quantity, i.e. the electric field value, its standard deviation and a coverage interval corresponding to a specific coverage probability (e.g. 95%). The use of this approach is particularly convenient when the conditions for applying the law of propagation of uncertainty are not fulfilled or its implementation is too complicate because of the complexity of the measurement model.

The basic idea of MCM is to assess the output uncertainty starting from a large number of random trials for each input quantity with a known probability density function (PDF), through a linear or non-linear model. The PDFs of the input quantities should be assigned on the basis of available knowledge (such as calibration data, experimental conditions and measurement experience).

The main stages of the uncertainty evaluation constitute:

(a) Establishing the model relating output Y quantity to the inputs $\mathbf{X}$

$$y = f(\mathbf{X})$$

where $\mathbf{X} = (X_1, X_2, \cdots X_W)^T$, W is the number of input quantities which are related to the measurand.

(b) Selecting a value M which refers to the number of Monte Carlo trials, i.e. the repeat times of model evaluation. Therefore, for each input quantity X_i, M draws are sampled through PDF $g_{X_i}(\xi_i)$.

The distribution function of X_i is defined as

$$G_{X_i}(\xi) = P_r(X_i \leq \xi_i)$$

where P_r represents the probability that the random variable X_i is less than or equal to ξ_i.

The Probability density function $g_{X_i}(\xi_i)$ for X_i is the derivation of the distribution function

$$g_{X_i}(\xi_i) = \mathrm{d}G_{X_i}(\xi_i)/\mathrm{d}\xi_i$$

where $g_{X_i}(\xi_i)\mathrm{d}\xi_i$ is the 'probability element'

$$g_{X_i}(\xi_i)\mathrm{d}\xi_i = P_r(\xi_i < X_i < \xi_i + \mathrm{d}\xi_i)$$

For the rth draw $\mathbf{x}_r$, the value of the model can be expressed as:

$$y_r = f(\mathbf{x}_r), r = 1, 2, \cdots, M$$

being vector $\mathbf{x}_r = (x_{1,r}, x_{2,r}, \cdots, x_{W,r})$. Here the input quantities $\mathbf{X}$ are assumed to be independent.

(c) Analyzing the output sequence $\{y\}^M$ in order to

1) find out the discrete representation $\mathbf{G}$ of the distribution function $G_Y(\eta)$, by firstly sorting the model values into non-decreasing order, which is denoted as

$$y_{(r)} = f(\mathbf{x}_r), r = 1, 2, \cdots, M.$$

The distribution function is $G_Y(\eta)$, and the corresponding PDF is $g_Y(\eta)$

An approximation of $g_Y(\eta)$ can be obtained through the normalized frequency histogram of discrete representation $\mathbf{G}$.

2) estimate the output quantity and its associated standard uncertainty.

The average of output sequence $\{y\}^M$ is

$$\widetilde{y} = \frac{1}{M}\sum_{r=1}^{M} y_r \tag{6.1}$$

and standard deviation $u^2(\widetilde{y})$ is determined from

$$u^2(\widetilde{y}) = \frac{1}{M-1}\sum_{r=1}^{M}(y_r - \widetilde{y})^2 \tag{6.2}$$

They are taken as an estimate y of Y and the standard uncertainty $u(y)$ associated with y.

3) and calculate the coverage interval of a specified coverage probability p for the output quantity.

Let $q = pM$, choose the closest integer for q. For any $r = 1, 2, \cdots, M - q$, $y_{low} = y_{(r)}$ and $y_{high} = y_{(r+q)}$. Then $[y_{low}, y_{high}]$ is a $100p\%$ coverage interval for Y. The shortest coverage interval is given by determining r^* such that, for $r = 1, 2, \cdots, M - q$, $y_{r^*+q} - y_{r^*} \leq y_{r+q} - y_r$.

This section takes reference from [55].

6.3 Electric field estimation procedure

With the reference to the proposed hybrid procedure, the uncertainty of the estimated electric field values comes from two main sources: the numerical approximation during the BEM reconstruction, and the magnetic field measurements performed over the virtual surface. These two uncertainty contributions can be evaluated separately since they can been assumed as uncorrelated.

The uncertainty contribution due to BEM reconstruction mainly depends on the number and distribution of the measurement points on the closed surface. The induced electric fields directly derived from the reconstructed field of Helmholtz coil system can be compared with those when the measurements on the box are replaced by the values evaluated through the Biot-Savart law, in order to evaluate the discrepancies from only the reconstruction procedure without the uncertainty contribution of measurement. After that, a statistical analysis should be performed to estimate the PDF. And finally, the two uncertainty components (measurement uncertainty and numerical approximation) must be combined together[56].

The following will focus on the measurement uncertainty estimate.

6.3.1 The input quantities

Since the magnetic fields are detected by an inductive probe with non-negligible dimensions (3 cm diameter coils) which is placed near the source where the spatial field distribution has a high non-uniformity, a small error in its position and orientation can give rise to sensible variation of the measured value. In order to simulate this situation, the field vector of the *n-th* measurement point is transformed into spherical coordinate as amplitude (H_n), title angle (Ψ_n) and orientation angle (Φ_n), so that the propagation distributions of positioning and rotation of the probe (which are the main input uncertainty of induction probe meters under presented circumstances) can be clearly quantified. The expectations of these three quantities for each measurement point are provided precisely by the simulative Helmholtz model introduced in Chapter 3 which applies directly Biot-Savart Law. The uncertainty component of the meter calibration has been disregarded because of its low level comparing the previous components when high field gradient presents in the measuring area.

Rectangular distributions are assigned to all the input quantities (H_n, Ψ_n and Φ_n) whose width is estimated on the basis of experimental data and the characteristics of the field meter. A specified procedure to determine the limits are provided in the last chapter.

Take the amplitude H_n as an example. A lower limit H_{na} and an upper limit H_{nb} with $H_{na} < H_{nb}$ has been chosen from available information. The PDF for H_n with a rectangular distribution $\mathrm{R}(H_{na}, H_{nb})$ is

$$g_X(\xi) = \begin{cases} 1/(H_{nb} - H_{na}) & H_{na} \leq \xi \leq H_{nb} \\ 0 & \text{otherwise} \end{cases} \tag{6.3}$$

where $n = 1, 2, \cdots, N$, N is the number of measurement points

For the sampling at *r-th* draw, assume that δ is randomly chosen from the standard rectangular distribution R(0,1)

$$H_n^r = H_{na} + (H_{nb} - H_{na})\delta \tag{6.4}$$

In a similar way, Ψ_n and Φ_n are sampled within $\mathrm{R}(\Psi_{na}, \Psi_{nb})$ and $\mathrm{R}(\Phi_{na}, \Phi_{nb})$ respectively.

The field vector must be transformed back into Cartesian Coordinate as input of the model. The field components at the n-th measurement point in t-th draw are expressed as

$$\begin{aligned} H^r_{xn} &= H^r_n cos(\Psi^r_n) cos(\Phi^r_n) \\ H^r_{yn} &= H^r_n cos(\Psi^r_n) sin(\Phi^r_n) \\ H^r_{zn} &= H^r_n sin(\Phi^r_n) \end{aligned} \tag{6.5}$$

6.3.2 The limits of input quantities for uncertainty estimate

The limits of title and orientation angles (Ψ_n and Φ_n, $n = 1, 2, ... \cdots, N$) mainly depend on the positioning system, especially the mechanical part that attaches the probe to the wooden frame enclosing the Helmholtz coils as shown in Figure 6.1.

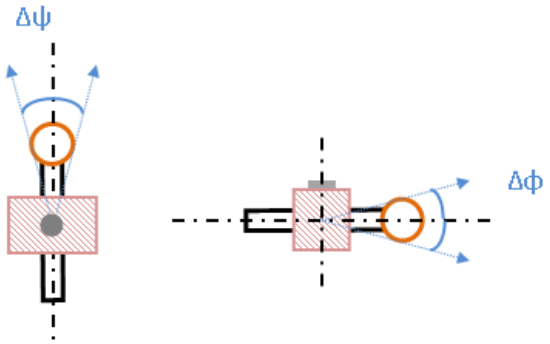

Figure 6.1: Rotations of the probe on the measuring wooden frame

The maximum rotating angles when the probe is fixed by this part during the measurement determine the upper and lower bands $\mathrm{R}(\Psi_{na}, \Psi_{nb})$ and $\mathrm{R}(\Phi_{na}, \Phi_{nb})$, which are both reasonably assumed to be $\mathrm{R}(-1°, 1°)$.

In order to evaluate the measurement variation limits of magnitude in a more general situation (e.g. industrial environment), repeated measurements were carried out without making use the positioning system.

Large amount of measurements have been performed before the determination of the limits of magnitudes (H_n, $n = 1, 2, ... \cdots, N$). The magnetic fields at various positions near the measuring frame have been detected repeatedly for several days. The average magnitudes of flux density (B_{ris}) and the normalization to the minimum field value for each point are calculated and reported in Table 6.1.

Date	No.	Position 1		Position 2	
		B_{ris}	Norm.	B_{ris}	Norm.
7/28/2012	1	25.76	0.00	31.33	0.00
7/29/2012	2	25.95	0.01	31.57	0.01
8/1/2012	3	26.16	0.02	32.33	0.03
8/2/2012	4	26.08	0.01	32.58	0.04
8/3/2012	5	26.05	0.01	32.68	0.04
8/5/2012	6	26.05	0.01	32.75	0.05
8/8/2012	7	26.09	0.01	32.79	0.05
8/9/2012	8	26.06	0.01	32.69	0.04
8/10/2012	9	26.08	0.01	32.66	0.04
8/18/2012	10	25.96	0.01	32.61	0.04
8/19/2012	11	26.17	0.02	32.79	0.05
8/22/2012	12	26.69	0.04	33.83	0.08

Table 6.1: Magnetic field (mT) in two points received from repeat measurement

Position 1 (0.0, 0.0, 2.7) locates near the center of one of the coils where the fields direct towards z direction, while Position 2 (0.3, 0.3, 2.7) is chosen to be close to the coil, where the fields are in high non-uniformity.

As shown in the table, at Position 1, the measurements have better performance in repeatability than at Position 2, where the largest deviation appears (about 8%). The magnitude limits for all the measurement points are set taken into consideration of the worst case.

6.3.3 An efficient numerical model

To obtain the induce electric field inside human model, the following conditions have been taken into account

- the energy of electric field generated by the source is negligible;
- the magnetic source is not significantly affected by stay effects;
- the human model is homogeneous
- the currents flowing within the human body do not modify the external magnetic field of the sources.

The magnetic fields measured over the virtual surface go through three steps, all of which possess the property of linearity:

(1) symmetry and fitting through radial basis function (interpolation) in order to receive the magnetic fields over the virtual surface;

(2) BEM procedure to reconstruct the magnetic field distribution in free space;

(3) BEM solution to compute the electric field inside the human model.

Making use of the linearity of the first two steps, the magnetic fields at any point outside the virtual surface can be treated as the superposition of those generated from each single measurement point, where the detected field vector can be expressed as unit vectors multiplied by certain coefficients. Furthermore, since the electric fields in any point inside human model rely on magnetic fields over the discrete body surface that provided from the second step, it can be received by evaluating the electric fields induced by magnetic fields in a single point located on the measuring frame, and then making a linear summation.

This means that a coefficient matrix can be configured, which allows to compute the electric fields directly through all the numerical steps for all samples. As a consequence, the computational procedure for error propagation can be performed by simply making a multiplication between a vector (of input magnetic fields) and a matrix.

At the position of *n-th* measurement point, impose a unite vector directs to one of the three field components (e.g. x-component), and zero to other components and all the other measurement points. The corresponding output of the model, a field vector at *t-th* test point inside human model is denoted as ($\mathbf{C}_{nx}^{t}$).

Repeat the process above for y and z components for this measurement point, so that the electric fields induced by the three components unite vectors ($\mathbf{C}_{nx}^{t}, \mathbf{C}_{ny}^{t}, \mathbf{C}_{nz}^{t}$) are obtained.

Repeat again the process for all the other $N-1$ points separately, until three matrix regarding to three field components ($\mathbf{C}_{x}^{t}, \mathbf{C}_{y}^{t}, \mathbf{C}_{z}^{t}$) are established. For number T text points,

$$\mathbf{C} = \begin{pmatrix} \mathbf{C}_x^1 & \mathbf{C}_y^1 & \mathbf{C}_z^1 & \cdots & \mathbf{C}_x^T & \mathbf{C}_y^T & \mathbf{C}_z^T \end{pmatrix} \tag{6.6}$$

the electric fields **E** for all the test points are

$$\mathbf{E} = \mathbf{H} \cdot \mathbf{C} \tag{6.7}$$

where **H** refers to the measured magnetic fields.

The scheme of proposed procedure adopted in MCM is shown in Figure 6.2.

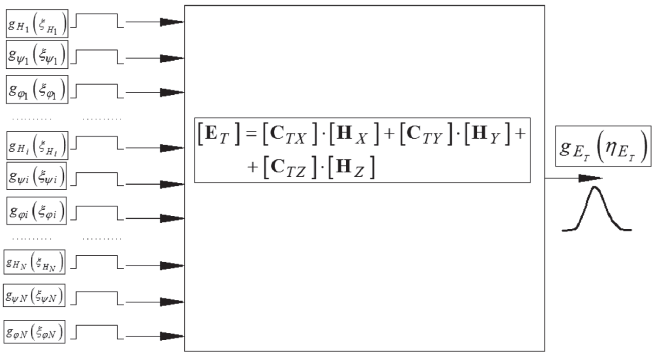

Figure 6.2: Scheme of the Monte Carlo procedure

6.3.4 Computation time

Monte Carlo Method is well known by its highly time-consuming feature. When it is applied to analyze the propagation of distributions, the computation time is taken up mainly by the following steps:

a) extraction procedure for all the input quantities (H_n, Ψ_n and Φ_n, $n = 1, 2, \cdots, N$)

b) computation of output through the adopted model for all the draws (normally $M \geq 10^5$)

c) sorting process to find out the probabilities distribution of the values of the model.

All the steps are encoded through FORTRAN 90, a widely used programming language to solve numerical problems. It has been also applied to the BEM reconstruction and electric field computation.

For steps a) and c), the computation time is almost fixed if certain parameters are given, such as the number of draws M, input quantities W and the computation speed of the processor. The programming method of extraction procedure follows Eq. 6.4.

However, time cost in step b) is various from different models. Assume that T_s is the duration when following the three steps (as described in the previous subsection) for one single extraction. The time spent in this step is

$$t_b = M \cdot T_s$$

If the simplified model in Eq. 6.7 is adopted instead, there needs only a multiplication operation, although, the preparation of the coefficient matrix in Eq. 6.6 must be taken into account. Thus, the duration becomes

$$t'_b \approx W \cdot N \cdot T_s + M \cdot T_{mtrx}$$

where T_{mtrx} refers to the operation time of matrix in Eq. 6.7. The contribution of the transformation procedure in Eq. 6.5 has been neglected. The ratio τ between the computation time of simplified model and original one is

$$\tau = \frac{t'_b}{t_b} = \frac{W \cdot N}{M} + \frac{T_{mtrx}}{T_s} \tag{6.8}$$

Here $M = 10^6$, $N = 45$, and $W = 3$. The size of T_{mtrx} depends on the number of measurement points as well as the test points. In any case, the computation would last within 100 ms, while T_s is more than 570 s. As a result, $\tau < 3 \times 10^{-4}$, which means the computation time can be reduced more than 3300 times with respect to the original model.

6.4 Results and discussion

Figure 6.3 shows the PDFs (input limits) of two test points obtained through MCM with 10^6 draws in two supply conditions (Supply α and β). The point at the height of 1.4 m is around the base of the neck of the human model, while point at 1.55 m is located inside the head.

The maximum induced electric field can be always found at the base of the neck as concluded in Chapter 5. In general, the PDFs of electric fields are quite symmetric and approximated a Gaussian distribution. Only under Supply α, it loses symmetry about at 1.55 m.

The peak value of the PDF indicates the most possible value for each test point.

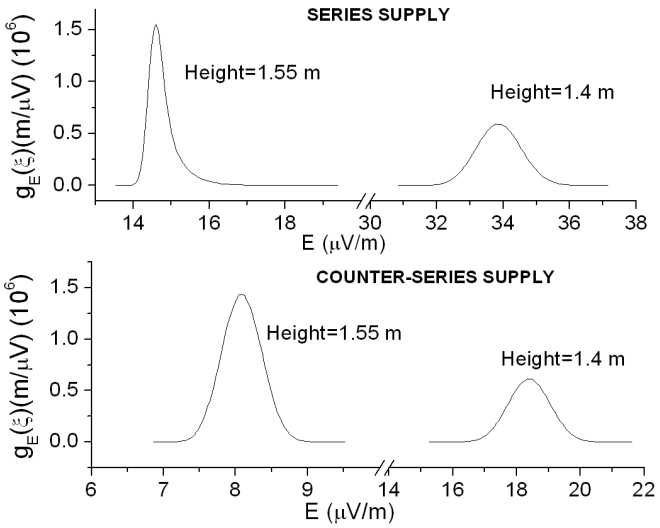

Figure 6.3: PDFs of electric field on two test points under Supply α and β

The average and associated standard uncertainty can be calculated following Eq. 6.1 and 6.2.

Table 6.2 lists the standard uncertainties as well as the estimate of the electric field when applying different limits H_{na} and H_{nb} for magnetic field amplitude H_n ($n = 1, 2, \cdots, 45$), in both supply conditions. 10% means the upper limit $H_{nb} = 1.1H_n$ and lower limit $H_{na} = 0.9H_n$, and so as 7% and 5%. Both limits for Ψ_n and Φ_n are assumed to be $\pm 1°$.

Supply	Height (m)	10%	7%	5%	E_{est} (μV/m)
α	1.55	2.6	1.5	0.9	15
	1.7	1.5	1.1	0.8	19
β	1.55	3.4	2.4	1.7	8
	1.7	3.3	2.4	1.7	10

Table 6.2: Relative standard uncertainties under different R(H_{na}, H_{nb})

The two test points investigated in the table are located inside the head of the human model. With smaller limit interval for H_n (which suggests smaller uncertainties of input), the uncertainty of induced electric field obviously decreases for both supply conditions. However, at same test point with same limits, the uncertainty under Supply β is always lager, while the estimated field values are lower in both test points,

comparing with Supply α.

The electric field has been estimated at nine test points along a vertical line inside human model, with the input limits $\pm 10\%$, $\pm 1°$and $\pm 1°$ for input quantities H_n, Ψ_n and Φ_n $(n = 1, 2, \cdots, 45)$. The limits are set taken into consideration the largest positioning error of the meter in on-site measurement.

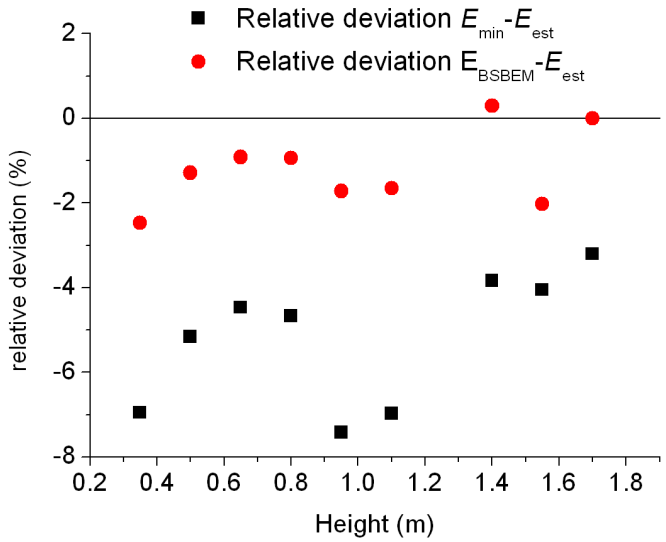

Figure 6.4: Comparison of relative deviation from E_{est} to E_{min} and E_{BSBEM}

The comparison of the relative deviation in Figure 6.4 is based on the electric field E_{est} estimated through the proposed method, through nine points along a vertical line inside the human model, under Supply α. The shortest coverage interval for each test point is evaluated with $p = 95\%$, where E_{min} represents the lower limit of the interval. E_{BSBEM} refers to the field computed when applying BEM only to compute the induced electric field, while the unperturbed magnetic field over the body surface is provided directly through Biot-Savart Law. The relative deviation from E_{est} suggests the uncertainty contribution of the discretization introduced by electric field prediction through BEM inside the human model.

As shown in the figure, the relative deviations from BSBEM always fall inside the left half of coverage interval ($\leq 2.3\%$) except at 1.4 m height, where E_{BSBEM} is 0.3% higher than estimate. Compared with the relative deviations from E_{min} which goes from 3.0% to 7.4%, the ones due to the BEM solution are 2% to 5% lower. It means

the measurement uncertainty contribution is the prevalent term, instead of the field reconstruction procedure.

It must be noticed that, when the limits of magnetic field amplitude H_n reduced to 5% or less as reported in Table 6.2, the relative deviations of BSBEM have the same level as the ones of measurement. In this case the uncertainty component of the BEM discretization must be taken into account for uncertainty estimate.

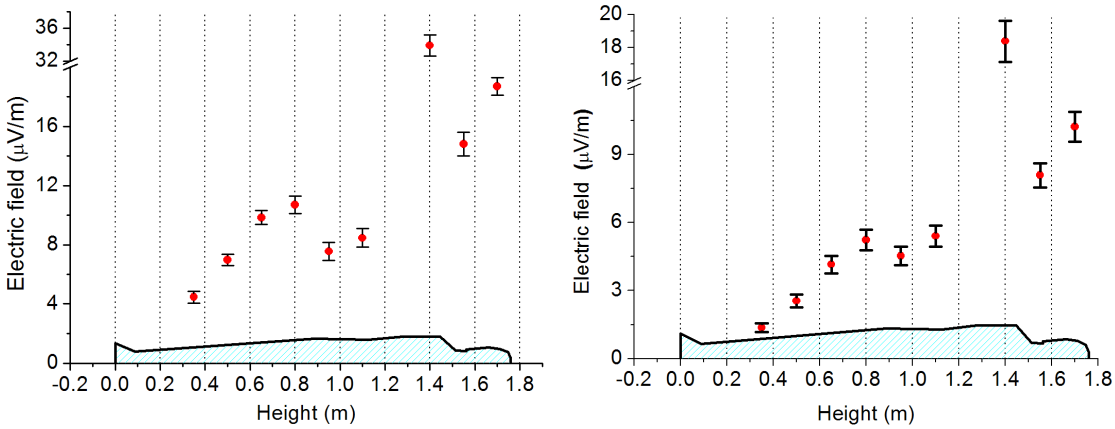

(a) Supply α **(b)** Supply β

Figure 6.5: Electric field and its coverage interval for Supply α and β

Figure 6.5 presents the distributions of the estimated electric field values and the corresponding coverage intervals in these nine points both under Supply α (in Figure 6.5a) and Supply β (in Figure 6.5b). The standard uncertainties are between 1.5% (under Supply α) and 7.3% (under Supply β). The uncertainty estimate of the electric field for all these points are listed in Chapter 8 for both supply conditions.

The experimental validation of the proposed simplified model has been carried out only through the magnetic field measured along the same vertical line but without human model's presence. The comparison in Figure 6.6 is between magnetic field and associated coverage interval estimated by propose model based on MCM, and the same quantities measured directly.

Here the input quantities for MCM are provided by real measurement instead of Biot-Savart Law. The standard uncertainties vary from 2.0% to 3.3%. Due to the low field level, the systematic errors due to the meters have been corrected taking into account the calibration data (calibration factor, from +3% to +7% depending

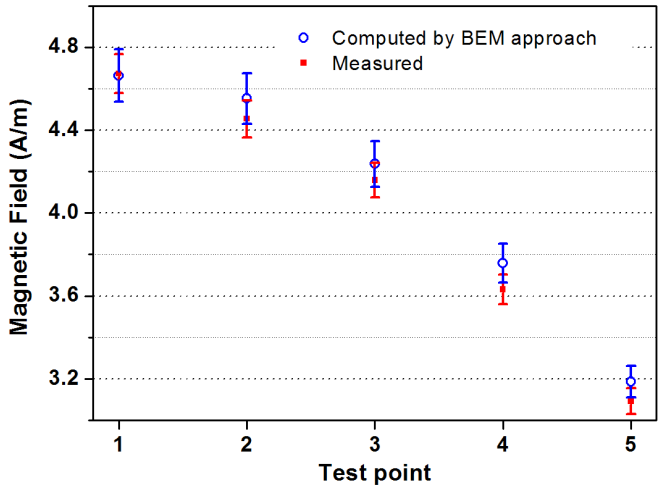

Figure 6.6: Comparison of magnetic fields between MCM and measurement

on the measured magnetic field value). The expanded uncertainty associated with measurement is estimated to be 2%.

7

Conclusions

A hybrid procedure aiming to reconstructing the field distributions generated by unknown sources and evaluating the internal electric fields inside a human model exposed to such sources has been proposed and explained in details.

At low frequency, the magnetic fields generated from a Helmholtz coil system have been well reconstructed by the measurements performed over a parallelepiped that includes both the coils, making use of intrinsic property of BEM. The induced electric fields inside the the model have been calculated by the field distributions over the external body surface, which are provided by the previous reconstruction procedure. The accuracy of both these two procedures have been investigated and good agreement with other evaluation approaches was found, especially when the field value is relatively high. Contribution of measurement uncertainty in this hybrid procedure is prevailing compared with the numerical one, under current measuring condition. Standard uncertainties of the estimated electric fields are various from 1.5% to 7.3%, depending on field distributions and investigating areas.

Next step of research in this frequency range should focus on more complicated sources, in order to bring this procedure to practical applications.

Same reconstruction procedure has been also validated at radio frequency, through a standardized validation procedure applied in EMC test. A good accuracy suggests that the proposed procedure has good perspective in the application of radiation emissions prediction. Experimental validation will be performed after the electric field probe in this frequency range is ready, which must be able to record the time behaviors for all the three field components.

8

Materials & methods

8.1 Vector Green's Theorem

Start from the vector identity:

$$\nabla \cdot (\mathbf{A} \times \mathbf{B}') = \mathbf{B}' \cdot \nabla \times \mathbf{A} - \mathbf{A} \cdot \nabla \times \mathbf{B}' \tag{8.1}$$

then substitute $\mathbf{B}'$ with $\nabla \times \mathbf{B}$ in Eq. 8.1,

$$\nabla \cdot (\mathbf{A} \times \nabla \times \mathbf{B}) = \nabla \times \mathbf{B} \cdot \nabla \times \mathbf{A} - \mathbf{A} \cdot \nabla \times \nabla \times \mathbf{B} \tag{8.2}$$

According to the divergence theorem, the net flux of some vector field $\mathbf{F}$ out of a surface $\partial\Omega$ which encloses the volume Ω can be related to the integral of the divergence of this vector as following:

$$\oint_{\partial\Omega} \mathbf{F} \cdot \mathbf{n} ds = \int_{\Omega} \nabla \cdot \mathbf{F} \tag{8.3}$$

where $\mathbf{n}$ is the normal unit vector directed outwards the volume Ω.

Impose $\mathbf{F} = \mathbf{A} \times \nabla \times \mathbf{B}$ in Eq. 8.3 , then Green's first identity in terms of vector is obtained:

$$\int_{\Omega} \nabla \cdot (\mathbf{A} \times \nabla \times \mathbf{B}) = \int_{\Omega} (\mathbf{A} \cdot \nabla \times \nabla \times \mathbf{B} - \nabla \times \mathbf{A} \cdot \nabla \times \mathbf{B}) dv = \oint_{\partial\Omega} \mathbf{A} \times \nabla \times \mathbf{B} \cdot \mathbf{n} ds \tag{8.4}$$

Since $\mathbf{A}$ and $\mathbf{B}$ are supposed to be two independent vectors inside volume Ω, interchange their positions in Eq. 8.4, it remains valid:

$$\int_{\Omega} (\mathbf{B} \cdot \nabla \times \nabla \times \mathbf{A} - \nabla \times \mathbf{B} \cdot \nabla \times \mathbf{A}) dv = \oint_{\partial\Omega} \mathbf{B} \times \nabla \times \mathbf{A} \cdot \mathbf{n} ds \tag{8.5}$$

The difference between Eq. 8.4 and Eq. 8.5 (Eq. 8.6) is Vector Green's Theorem [57]:

$$\int_{\Omega}(\mathbf{B}\cdot\nabla\times\nabla\times\mathbf{A}-\mathbf{A}\cdot\nabla\times\nabla\times\mathbf{B})dv=\oint_{\partial\Omega}(\mathbf{A}\times\nabla\times\mathbf{B}-\mathbf{B}\times\nabla\times\mathbf{A})\cdot\mathbf{n}ds \quad (8.6)$$

8.2 Magnetic field distributions of Helmholtz coils

In Figure 8.1, there are the simulative magnetic flux density distributions with serial and parallel connections (corresponding to Supply α and β)

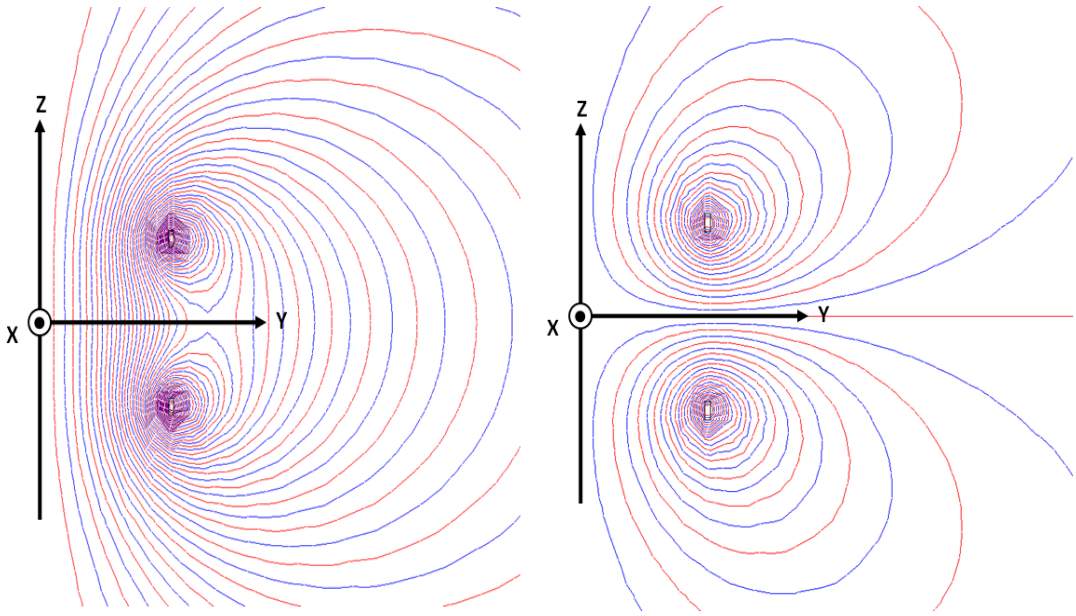

(a) Serial connection (Supply α) **(b)** Parallel connection (Supply β)

Figure 8.1: Magnetic field distributions of Helmholtz coils

Since the fields produced from these two connections are both cylindrical symmetric about the main axis (z axis), the distributions along x and y axises are the same.

8.3 The transformation of the coordinates

The internal sensor of the probe of the field meter ELT-400 are arranged orthogonally. Its coordinate system is designed to detect equal field strength along the three axises of when the fields parallel to its central axis. The y-axis is perpendicular to the horizontal plan when the probe is configured as illustrated on the left in Figure 8.2 (side view). Both x-axis and z-axis oriented at equal angle θ to the central axis of the probe.

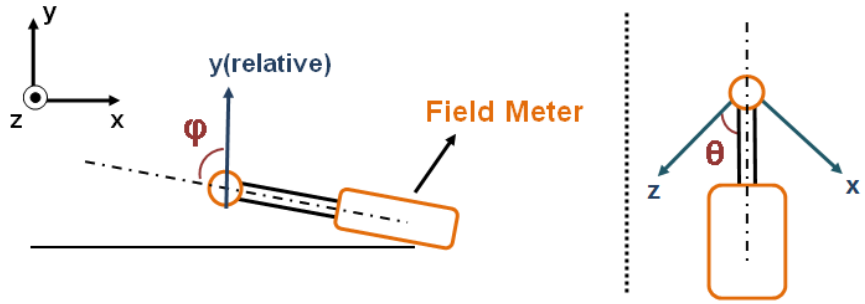

Figure 8.2: 3 cm^2 cross-sectional area magnetic filed probe layout for ELT-400

During the measurements around the Helmholtz coils system, the probe will be positioned on 5 different relative coordinates on the wooden measurement frame referring to the common spacial axes (Figure 8.3).

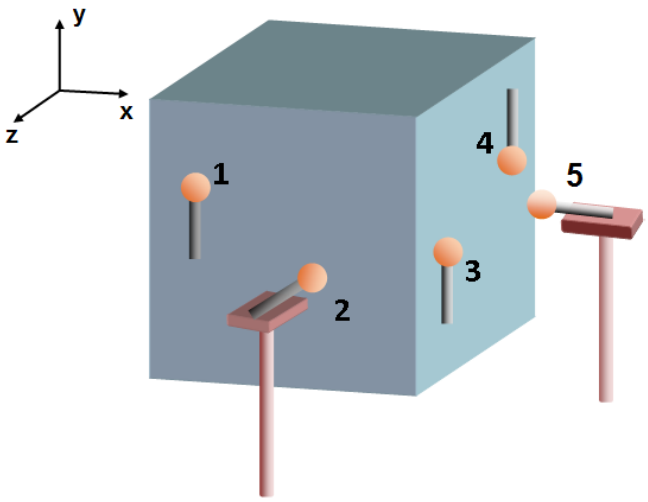

Figure 8.3: Relative positions of the probe in the measurements

With Position 1, the probe measures the field distribution in Region A (as indicated

in Figure 4.3). With 3 and 4 it measures in Region B. Position 2 and 5 locates outside the virtual surface for the investigation of the reconstruction accuracy.

Table 8.1 lists the transformation equations from all the five relative coordinates to the common one applied on both the virtual surface and the Helmholtz coils system.

Position index	Transformation equations
1	$x_{co} = (x_{re1} - z_{re1})\cos\theta$
	$y_{co} = y_{re1}\cos\varphi + (x_{re1} + z_{re1})\cos\theta\sin\varphi$
	$z_{co} = y_{re1}\sin\varphi - (x_{re1} + z_{re1})\cos\theta\cos\varphi$
2	$x_{co} = (z_{re2} + x_{re2})\cos\theta$
	$y_{co} = y_{re2}\sin\varphi - (z_{re2} - x_{re2})\sin\theta\cos\varphi$
	$z_{co} = y_{re2}\cos\varphi + (z_{re2} - x_{re2})\sin\theta\sin\varphi$
3	$x_{co} = y_{re3}\sin\varphi - (x_{re3} + z_{re3})\cos\theta\cos\varphi$
	$y_{co} = y_{re3}\cos\varphi + (x_{re3} + z_{re3})\cos\theta\sin\varphi$
	$z_{co} = (z_{re3} - x_{re3})\cos\theta$
4	$x_{co} = y_{re4}\sin\varphi - (x_{re4} + z_{re4})\cos\theta\cos\varphi$
	$y_{co} = -y_{re4}\cos\varphi - (x_{re4} + z_{re4})\cos\theta\sin\varphi$
	$z_{co} = (x_{re4} - z_{re4})\cos\theta$
5	$x_{co} = -y_{re5}\cos\varphi - (x_{re5} - z_{re5})\cos\theta\sin\varphi$
	$y_{co} = y_{re5}\sin\varphi - (x_{re5} - z_{re5})\cos\theta\cos\varphi$
	$z_{co} = (x_{re5} + z_{re5})\sin\theta$

Table 8.1: The transformation of the coordinates

In the Table, the subscript *co* refers to the common coordinate system, while $re + index$ means the relative coordinate system for each position.

8.4 The symmetry of field distributions around Helmholtz system

After the measurement of 45 points on the two quarters of two surfaces of the virtual parallelepiped through the wooden support frame, there are two steps to achieve 488 points distributed over all the surfaces as the input of the BEM reconstruction procedure.

The first step is to perform the symmetry on the same surfaces as the measured points. Figure 8.4 illustrates the method in order to obtain the field distributions on

the other three quarters of the Surface A under Supply α.

Take the original measurement points located in Region A (right up quarter) as references, with '+' it means keeping the sign of the field vector as reference in such quarter, while with '−', the field vector should be reversed.

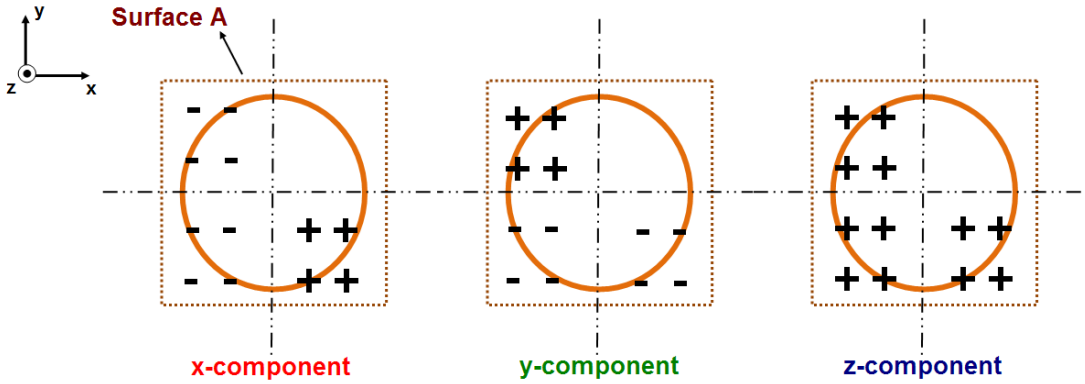

Figure 8.4: The symmetry of the filed vectors on Surface A with Supply α

The x and y components can be obtained by the symmetry about the y and then x axises. For z component, it should remain the same all over the surface. As for the other two supply conditions (Supply β and γ), the same method has been applied on Surface A.

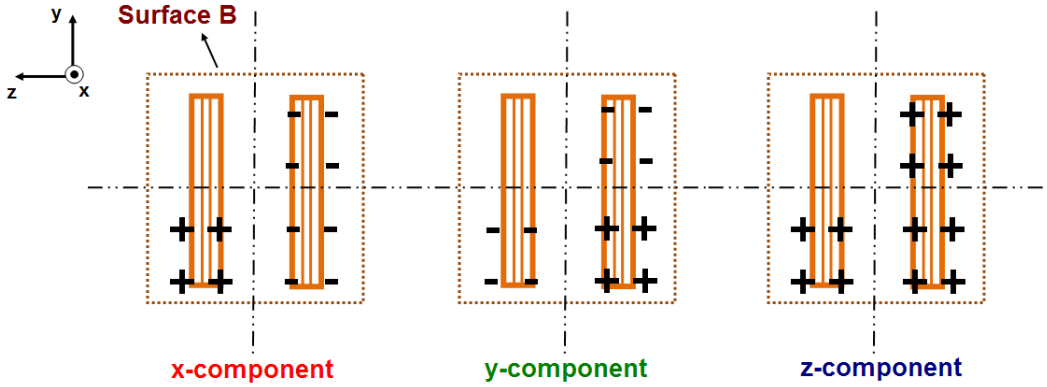

Figure 8.5: The symmetry of the filed vectors on Surface B with Supply α

On Surface B, as illustrated in Figure 8.5, the z component behaves the same as on Surface A. In stead, along x component, the two coils produce opposite fields with Supply α, and in y component, the fields differ in the upper two quarters and the lower

ones and also in left and right ones.

The field distributions on the other four surfaces can be received from A and B, as reported in Table 8.2. Surface C is symmetric with A about $z = 0$ plan and D is symmetric with C about $x = 0$. The subscript indicates the field component on such surface.

Surface	Symmetry equations
C	$x_C = -x_A$
	$y_C = -y_A$
	$z_C = z_A$
D	$x_D = -x_B$
	$y_D = y_B$
	$z_D = z_B$
E	$x_E = y_B$
	$y_E = x_B$
	$z_E = z_B$
F	$x_F = x_E$
	$y_F = -y_E$
	$z_F = z_E$

Table 8.2: The symmetry among the surfaces with Supply α

As for Surface B under Supply β, the fields distribute quite differently due to the opposite supply currents flowing in the two coils. Figure 8.6 illustrates the symmetry method of the field vectors over the Surface B.

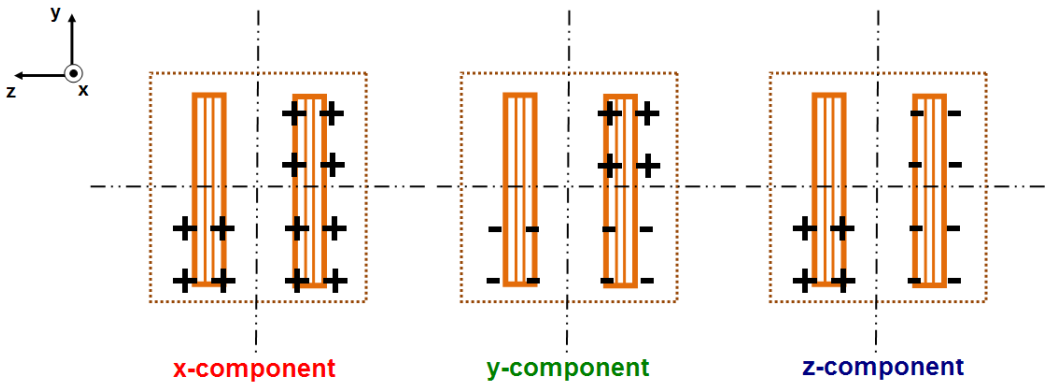

Figure 8.6: The symmetry of the filed vectors on Surface B with Supply β

Among the other 4 surfaces, the symmetry is almost the same as listed in Table 8.2 except on Surface C where all the field components have opposite direction to Surface A comparing with Supply α.

As a matter of fact, the field distributions under Supply γ is a combination of those under Supply α and β. Suppose the supply current flowing in the two coils are $I_1 = I\sin(\omega_1 x + \phi_1)$ and $I_2 = I\sin(\omega_2 x + \phi_2)$ under Supply α. The resultant fields are the superposition of those produced by current I_1 and I_2 respectively. With Supply β, the linear summation is between I_1 and $-I_2$, under the assumption that the current values are identical to Supply α, which can be easily realized by the supply circuit. The field distributions of No.1 coil $\mathbf{H_1}$ while supplied with I_1 can be received from the ones under Supply α ($\mathbf{H}_\alpha$) and β($\mathbf{H}_\beta$) by Eq. 8.7

$$\mathbf{H_1} = \frac{\mathbf{H}_\alpha + \mathbf{H}_\beta}{2} \tag{8.7}$$

In the same way, the field distributions of No.2 coil $\mathbf{H_2}$ under supply of I_2 are

$$\mathbf{H_2} = \frac{\mathbf{H}_\alpha - \mathbf{H}_\beta}{2} \tag{8.8}$$

With various combinations of the field distributions from each coil, plenty kinds of resultant fields can be received. When the current supplied the No.2 coil has a 90 ° shift as shown in Figure 3.2, it means the field vectors rotate from real to imaginary. As a result, the field distributions under Supply γ are

$$\mathbf{H}_\gamma = \mathbf{H_1} + \mathbf{H_2}i \ = \frac{\mathbf{H}_\alpha + \mathbf{H}_\beta}{2} + \frac{\mathbf{H}_\alpha - \mathbf{H}_\beta}{2}i \tag{8.9}$$

8.5 Electric field uncertainties

The induced electric field uncertainty estimated through Monte Carlo Method are reported in Table 8.3 and 8.4, along the same vertical line as shown in Figure 6.5. The input quantities have limits ±10%, ±1°and ±1° with rectangular distributions.

Height (m)	E_{est} (μV/m)	Standard uncertainty (%)	Coverage interval ($p = 95\%$)
0.35	4.46	4.1	[4.15, 4.85]
0.5	6.98	2.7	[6.62, 7.37]
0.65	9.84	2.3	[9.40, 10.3]
0.8	10.7	2.5	[10.2, 11.3]
0.95	7.55	3.9	[6.99, 8.15]
1.1	8.46	3.7	[7.87, 9.09]
1.4	33.9	2.0	[32.6, 35.2]
1.55	14.8	2.6	[14.2, 15.6]
1.7	18.7	1.5	[18.1, 19.3]

Table 8.3: Uncertainty estimate of electric field in supply condition α

Under Supply α, the relative uncertainty of estimated electric field is from 1.5% to 4.1%, while under Supply β, it reaches 7.3% when the electric field is lower than 1.5 $\mu V/m$.

Height (m)	E_{est} (μV/m)	Standard uncertainty (%)	Coverage interval ($p = 95\%$)
0.35	1.37	7.3	[1.18, 1.56]
0.5	2.54	5.7	2.26, 2.82
0.65	4.15	4.7	3.77, 4.54
0.8	5.23	4.4	4.78, 5.68
0.95	4.53	4.7	4.12, 4.95
1.1	5.41	4.4	4.94, 5.88
1.4	18.4	3.5	17.2, 19.6
1.55	8.09	3.4	7.56, 8.62
1.7	10.2	3.3	9.56,10.9

Table 8.4: Uncertainty estimate of electric field in supply condition β

References

[1] A. Gérin, B. Stockbroeckx, and A. Vander Vorst. **Champs micro-ondes et santé**. Technical report, Faculte Polytechnique de Mons, Electromagnetisme et Telecommunications, 1999. 1

[2] E.C. Jordan and K.G. Balmain. *Electromagnetic waves and radiating systems*. Prentice-Hall, 1950. 2

[3] A. Vander Vorst, A. Rosen, and Y. Kotsuka. **RF/Microwave interaction with biological tissues**. *RF/Microwave Interaction with Biological Tissues, by André Vander Vorst, Arye Rosen, Youji Kotsuka, pp. 384. Wiley-VCH, December 2005.* 2

[4] J.P. Reilly. *Applied bioelectricity: from electrical stimulation to electropathology*. Springer Verlag, 1998. 2

[5] J.P. Reilly. **Neuroelectric mechanisms applied to low frequency electric and magnetic field exposure guidelines-Part I: Sinusoidal waveforms**. *Health physics*, **83**(3):341–355, 2002. 2

[6] D. Attwell. **Interaction of low frequency electric fields with the nervous system: the retina as a model system**. *Radiation protection dosimetry*, **106**(4):341–348, 2003. 2

[7] ICNIRP. **Guidelines for limiting exposure to time-varying electric, magnetic, and electromagnetic fields (up to 300 GHz)**. *Health physics*, **74**(4):494–522, 1998. 2

[8] ICNIRP. **Guidelines for limiting exposure to time-varying electric and magnetic fields (1 Hz to 100 kHz)**. *Health physics*, **99**(6):818–836, 2010. 3

[9] ICNIRP. **Statement on the Guidelines for limiting exposure to time-varying electric, magnetic and electromagnetic fields (up to 300 GHz)**. *Health physics*, **97**(3):257–259, 2009. 3

[10] ICRP. **Human Respiratory Tract Model for Radiological Protection. ICRP Publication 66**. *Ann.*, **24**(1–3), 1994. 3

REFERENCES

[11] D.W. Deno. **Currents induced in the human body by high voltage transmission line electric field -Measurement and calculation of distribution and dose**. *IEEE Transactions on Power Apparatus and Systems*, **96**(5):1517 – 1527, Sept. 1977. 3

[12] DW Deno. **Monitoring of personnel exposed to a 60-Hz electric field**. *Biological Effects Extremely Low Frequency Electromagnetic Fields*, 1979. 3

[13] WT Kaune and WC Forsythe. **Current densities measured in human models exposed to 60-Hz electric fields**. *Bioelectromagnetics*, **6**(1):13–32, 1985. 3

[14] D.L. Miller. **Miniature-probe measurements of electric fields and currents induced by a 60-Hz magnetic field in rat and human models**. *Bioelectromagnetics*, **12**(3):157–171, 1991. 4

[15] PM Glover and R. Bowtell. **Measurement of electric fields due to time-varying magnetic field gradients using dipole probes**. *Physics in medicine and biology*, **52**(17):5119, 2007. 4

[16] P M Glover and R Bowtell. **Measurement of electric fields induced in a human subject due to natural movements in static magnetic fields or exposure to alternating magnetic field gradients**. *Physics in medicine and biology*, **53**(2):361, 2008. 4

[17] P. Dimbylow and R. Findlay. **The effects of body posture, anatomy, age and pregnancy on the calculation of induced current densities at 50 Hz**. *Radiation protection dosimetry*, **139**(4):532–538, 2010. 4

[18] A. Hirata, K. Wake, S. Watanabe, and M. Taki. **In-situ electric field and current density in Japanese male and female models for uniform magnetic field exposures**. *Radiation protection dosimetry*, **135**(4):272–275, 2009. 4

[19] Y. Li, J.W. Hand, T. Wills, and J.V. Hajnal. **Numerically-simulated induced electric field and current density within a human model located close to az-gradient coil**. *Journal of Magnetic Resonance Imaging*, **26**(5):1286–1295, 2007. 4

[20] O. Bottauscio, M. Chiampi, and L. Zilberti. **Boundary element approaches for the evaluation of human exposure to low frequency electromagnetic fields**. *IEEE Transactions on Magnetics*, **45**(3):1674–1677, 2009. 4

[21] M. Nadeem, T. Thorlin, O.P. Gandhi, and M. Persson. **Computation of electric and magnetic stimulation in human head using the 3-D impedance method**. *IEEE Transactions on Biomedical Engineering*, **50**(7):900–907, 2003. 4

[22] W. Xi, M.A. Stuchly, and O.P. Gandhi. **Induced electric currents in models of man and rodents from 60 Hz magnetic fields**. *IEEE Transactions on Biomedical Engineering*, **41**(11):1018–1023, 1994. 4

[23] S. Fiori, A. Faba, L. Albini, E. Cardelli, and P. Burrascano. **Numerical modeling for the localization and the assessment of electromagnetic field sources**. *IEEE Transactions on Magnetics*, **39**(3):1638 – 1641, may 2003. 5

[24] S. Coco, A. Laudani, and L. Mazzurco. **A novel 2-D ray tracing procedure for the localization of EM field sources in urban environment**. *IEEE Transactions on Magnetics*, **40**(2):1132–1135, 2004. 5

[25] G. Crevecoeur, H. Hallez, L. Dupré, R. Van de Walle, P. Boon, and I. Lemahieu. **Validation of the two-level approach for the solution of the EEG inverse problem in an anisotropic realistic head model**. *IEEE Transactions on Magnetics*, **45**(3):1670–1673, 2009. 5

[26] F. Luan, J.H. Choi, C. Lee, M.H. Kim, and H.K. Jung. **Precise Estimation of Correlated Bio-Electromagnetic Activities in Deep Source Space**. *IEEE Transactions on Magnetics*, **48**(2):339–342, 2012. 5

[27] C. Cobos Sánchez, H. Power, S.G. Garcia, and A. Rubio Bretones. **Quasi-static multi-domain inverse boundary element method for MRI coil design with minimum induced E-field**. *Engineering Analysis with Boundary Elements*, **35**(3):264–272, 2011. 5

[28] C.C. Sánchez, M.F. Pantoja, and R.G. Martín. **Design of Gradient Coil for Magnetic Resonance Imaging Applying Particle-Swarm Optimization**. *IEEE Transactions on Magnetics*, **47**(12):4761–4768, 2011. 5

[29] K. Yamazaki and T. Kawamoto. **Simple estimation of equivalent magnetic dipole moment to characterize ELF magnetic fields generated by electric appliances incorporating harmonics**. *IEEE Transactions on Electromagnetic Compatibility*, **43**(2):240–245, 2001. 5

[30] A. Canova, F. Freschi, M. Repetto, and M. Tartaglia. **Identification of an equivalent-source system for magnetic stray field evaluation**. *IEEE Transactions on Power Delivery*, **24**(3):1352–1358, 2009. 5

[31] O. Bottauscio, M. Chiampi, and L. Zilberti. **A boundary element approach to relate surface fields with the specific absorption rate (SAR) induced in 3-D human phantoms**. *Engineering Analysis with Boundary Elements*, **35**(4):657–666, 2011. 5

[32] International Electrotechnical Commission et al. **CISPR 22 Information Technology EquipmentRadio Disturbance CharacteristicsLimits and Methods of Measurement**. *Geneva, Switzerland: CISPR2008*, 2005. 5

[33] S. Mazzola. **MIL-STD-461: The basic military EMC specification and it's evolution over the years**. In *Systems, Applications and Technology Conference, 2009. LISAT '09. IEEE Long Island*, pages 1–5, May 2009. 5

[34] EN 50383. **Basic standard for the calculation and measurement of electromagnetic field strength and SAR related to human exposure from radio base stations and fixed terminal stations for wireless telecommunication systems (110 MHz-40 GHz)**. *European Committee for Electrotechnical Standardisation (CENELEC)*, 2010. 5

[35] H. Weng, D.G. Beetner, and R.E. DuBroff. **Prediction of radiated emissions using near-field measurements**. *Electromagnetic Compatibility, IEEE Transactions on*, **53**(4):891–899, 2011. 5

[36] T.K. Sarkar and A. Taaghol. **Near-field to near/far-field transformation for arbitrary near-field geometry utilizing an equivalent electric current and MoM**. *Antennas and Propagation, IEEE Transactions on*, **47**(3):566–573, 1999. 5

[37] T.B. Hansen. **Formulation of spherical near-field scanning for electromagnetic fields in the time domain**. *Antennas and Propagation, IEEE Transactions on*, **45**(4):620–630, 1997. 5

[38] P. Dimbylow. **Development of the female voxel phantom, NAOMI, and its application to calculations of induced current densities and electric fields from applied low frequency magnetic and electric fields**. *Physics in medicine and biology*, **50**(6):1047, 2005. 8

[39] P. Dimbylow. **Development of pregnant female, hybrid voxel-mathematical models and their application to the dosimetry of applied magnetic and electric fields at 50 Hz**. *Physics in medicine and biology*, **51**(10):2383, 2006. 8

[40] EN 62226-3-1:2005. **Exposure to electric or magnetic fields in the low and intermediate frequency range-Methods for calculating the current density and internal electric field induced in the human body Part 3-1: Exposure to electric fields Analytical and 2D numerical models**. *European Committee for Electrotechnical Standardisation (CENELEC)*, 2005. 8

[41] R.S. Elliot. *Electromagnetics: history, theory, and applications*. IEEE, 1993. 11

[42] Luca Zilberti. *Computational models for the evaluation of human exposure to electromagnetic fields*. Politecnico di Torino, 2010. 12

[43] C.R. Paul, K.W. Whites, and S.A. Nasar. *Introduction to Electromagnetic Fields*. McGraw-Hill series in electrical and computer engineering: Electromagnetics. WCB/McGraw-Hill, 1998. 18

[44] MSC Software Corporation. **Complete FEA Modeling Solution**. 20

[45] Nam Mai-Duy and Thanh Tran-Cong. **Approximation of function and its derivatives using radial basis function networks**. *Applied Mathematical Modelling*, **27**(3):197 – 220, 2003. 24, 25

[46] M. Chiampi, G. Crotti, and D. Giordano. **Set Up and Characterization of a System for the Generation of Reference Magnetic Fields From 1 to 100 kHz**. *IEEE Transactions on Instrumentation and Measurement*, **56**(2):300 –304, April 2007. 27

[47] W. Wang, O. Bottauscio, M. Chiampi, D. Giordano, and L. Zilberti. **An experimental-computational technique for evaluating magnetic field distributions around unknown sources**. *IEEE Transactions on Magnetics*, DOI 10.1109/TMAG.2012.2217751. 45

[48] W. Wang, O. Bottauscio, M. Chiampi, D. Giordano, and L. Zilberti. **A procedure to estimate the electric field induced in human body exposed to unknown magnetic sources**. *Radiation Protection Dosimetry*, DOI: 10.1093/rpd/ncs168. 49

[49] Computer Simulation Technology. **CST MICROWAVE STUDIO**. 55

[50] M. Borsero, O. Bottauscio, L. Zilberti, M. Chiampi, and W. Wang. **A boundary element estimate of radiated emissions produced by unknown sources**. In *2012 International Symposium on Electromagnetic Compatibility (EMC EUROPE)*, pages 1–6, Sept. 2012. 55

[51] CISPR22. **Information technology equipment – Radio disturbance characteristics – Limits and methods of measurement**. *IEC*, 2008. 55

[52] A. Bahr, T. Bolz, and C. Hennes. **Numerical dosimetry ELF: accuracy of the method, variability of models and parameters, and the implication for quantifying guidelines**. *Health physics*, **92**(6):521–530, 2007. 61

[53] J.M. Paniagua, M. Rufo, A. Jimenez, A. Antolín, and F.T. Pachon. **Estimation of Uncertainties in Electric Field Exposure From Medium-Frequency AM Broadcast Transmitters**. *IEEE Transactions on Instrumentation and Measurement*, **61**(1):122–128, 2012. 61

[54] IEC BIPM, ISO IFCC, and I. IUPAC. **OIML. Evaluation of measurement data Guide to the expression of uncertainty in measurement JCGM 100: 2008 (GUM 1995 with minor corrections)**. *BIPM Joint Committee for Guides in Metrology, Paris, Sfievres*, 2008. 61

[55] IEC BIPM, ISO IFCC, and I. IUPAC. **OIML 2008 Evaluation of Measurement Data–Supplement 1 to the "Guide to the Expression of Uncertainty in Measurement" –Propagation of distributions using a Monte Carlo method**. *BIPM Joint Committee for Guides in Metrology, Paris, Sfievres*, 2008. 64

REFERENCES

[56] Gabriella Crotti, Oriano Bottauscio, Mario Chiampi, Domenico giordano, Wencui Wang, and Luca Zilbertii. **Uncertainty Estimate Associated to the Electric Field Induced inside Human Bodies by Unknown LF Sources**. *IEEE Transactions on Instrumentation and Measurement*, DOI: 10.1109/TIM.2012.2230812. 64

[57] JA Stratton and LJ Chu. **Diffraction theory of electromagnetic waves**. *Physical Review*, **56**(1):99, 1939. 78